DUST OBSCURATION AND METALLICITY AT HIGH REDSHIFT: NEW INFERENCES FROM UV, Hα, AND 8 μm OBSERVATIONS OF $z \sim 2$ STAR-FORMING GALAXIES

2010 ApJ 712 1070

(http://iopscience.iop.org/0004-637X/712/2/1070)

The Astrophysical Journal, 712:1070–1091, 2010 April 1 doi:10.1088/0004-637X/712/2/1070

DUST OBSCURATION AND METALLICITY AT HIGH REDSHIFT: NEW INFERENCES FROM UV, Hα, AND 8 μm OBSERVATIONS OF $z \sim 2$ STAR-FORMING GALAXIES*

Naveen A. Reddy[1,7], Dawn K. Erb[2,8], Max Pettini[3,4], Charles C. Steidel[5], and Alice E. Shapley[6]
[1] National Optical Astronomy Observatory, 950 N Cherry Ave., Tucson, AZ 85719, USA
[2] University of California at Santa Barbara, Santa Barbara, CA 93106, USA
[3] Institute of Astronomy, Madingley Road, Cambridge CB3 OHA, UK
[4] International Centre for Radio Astronomy Research, University of Western Australia, 35 Stirling Highway, Crawley, WA 6009, Australia
[5] California Institute of Technology, MS 105–24, Pasadena, CA 91125, USA
[6] University of California at Los Angeles, 430 Portola Plaza, Box 951547, Los Angeles, CA 90095, USA
Received 2009 October 27; accepted 2010 February 3; published 2010 March 10

ABSTRACT

We use a sample of 90 spectroscopically confirmed Lyman break galaxies with Hα measurements and *Spitzer* MIPS 24 μm observations to constrain the relationship between rest-frame 8 μm luminosity (L_8) and star formation rate (SFR) for L^* galaxies at $z \sim 2$. We find a tight correlation with 0.24 dex scatter between L_8 and Hα luminosity/SFR for $z \sim 2$ galaxies with $10^{10}\ L_\odot \lesssim L_{\rm IR} \lesssim 10^{12}\ L_\odot$. Employing this relationship with a larger sample of 392 galaxies with spectroscopic redshifts, we find that the UV slope β can be used to recover the dust attenuation of the vast majority of moderately luminous L^* galaxies at $z \sim 2$ to within a 0.4 dex scatter using the local correlation. Separately, young galaxies with ages $\lesssim$100 Myr appear to be less dusty than their UV slopes would imply based on the local trend and may follow an extinction curve that is steeper than what is typically assumed. Consequently, very young galaxies at high redshift may be significantly less dusty than inferred previously. Our results provide the first direct evidence, *independent of the UV slope*, for a correlation between UV and bolometric luminosity ($L_{\rm bol}$) at high redshift, in the sense that UV-faint galaxies are on average less infrared and less bolometrically luminous than their UV-bright counterparts. The $L_{\rm bol}$–$L_{\rm UV}$ relation indicates that as the SFR increases, $L_{\rm UV}$ turns over (or "saturates") around the value of L^* at $z \sim 2$, implying that dust obscuration may be largely responsible for modulating the bright end of the UV luminosity function. Finally, dust attenuation is found to correlate with oxygen abundance at $z \sim 2$. Accounting for systematic differences in local and high-redshift metallicity calibrations, we find that L^* galaxies at $z \sim 2$, while at least an order of magnitude more bolometrically luminous, exhibit ratios of metals to dust that are similar to those of local starbursts. This result is expected if high-redshift galaxies are forming their stars in a less metal-rich environment compared to local galaxies of the same luminosity, thus naturally leading to a redshift evolution in both the bolometric luminosity–metallicity and bolometric luminosity–obscuration relations.

Key words: dust, extinction – galaxies: abundances – galaxies: evolution – galaxies: high-redshift – infrared: galaxies

Online-only material: color figures

1. INTRODUCTION

Quantifying the total energetics and the time evolution of the dust properties of high-redshift galaxies requires an understanding of the extent to which the locally calibrated relations between mid-infrared (rest-frame 8 μm) and bolometric luminosity apply at high redshift. The *Spitzer Space Telescope* allows for a direct measure of the mid-IR dust emission from typical (L^*) galaxies at $z > 1.5$ and has motivated a number of investigations of the correlation between mid-IR and bolometric luminosity. The mid-IR emission from 5–8.5 μm (rest-frame) arises from the stochastic UV photo-heating of small dust grains and polycyclic aromatic hydrocarbons (PAHs; e.g., Puget & Leger 1989; Tielens et al. 1999). As such, this emission is found to correlate with the UV radiation from OB stars and hence the global star formation rate (SFR) in nearby galaxies (e.g., Förster Schreiber et al. 2004; Roussel et al. 2001), albeit with some variation depending on metallicity and ionizing hardness (e.g., Engelbracht et al. 2005; Hogg et al. 2005; Helou et al. 2001; Normand et al. 1995). More recently, Kennicutt et al. (2009) demonstrate for the local *SINGS* sample of galaxies the general agreement between Balmer-decrement dust-corrected Hα SFRs and those derived by combining tracers of obscured star formation, including IR and 8 μm luminosity, and tracers of unobscured star formation (observed Hα luminosity).

At high redshift, several studies suggest that on average the ratios of mid to total infrared luminosity for luminous 24 μm-selected star-forming galaxies at $z \sim 2$ are larger than those found for local galaxies with similar bolometric luminosities (Papovich et al. 2007; Rigby et al. 2008). On the other hand, X-ray and radio stacking analyses suggest that the correlation between mid-IR and infrared luminosity for the less luminous but more typical galaxies at $z \sim 2$ (i.e., those with luminosities comparable to $L^*_{\rm UV}$ or $L^*_{\rm bol}$ at $z \sim 2$; Reddy et al. 2008; Reddy & Steidel 2009) is consistent with the local relations (Reddy et al. 2006b; Reddy & Steidel 2004). Taken together, these results imply a luminosity dependence in the correlation between mid-IR and bolometric luminosity.

While progress in connecting the dust emission of high-redshift galaxies to their bolometric luminosities can be informative, most $z > 3$ galaxies are selected via the efficient UV-dropout technique (Steidel et al. 1995) and tend to be too faint and at too high redshift to be detected directly via their dust emission. Thus, it has become common to rely on UV-based

* Based, in part, on data obtained at the W.M. Keck Observatory, which is operated as a scientific partnership among the California Institute of Technology, the University of California, and NASA, and was made possible by the generous financial support of the W.M. Keck Foundation.
[7] Hubble Fellow.
[8] Spitzer Fellow.

inferences of the dust attenuation and bolometric SFRs of $z > 3$ galaxies that require some assumption of how the rest-frame UV slope varies with extinction. The highest redshift where the correlation between UV slope and dust extinction has been tested for large numbers of spectroscopically confirmed galaxies is at $z \sim 2$. The results suggest that the local relation between UV slope and extinction remains valid at $z \sim 2$ for galaxies with moderate bolometric luminosities similar to those of luminous infrared galaxies, or LIRGs (Reddy et al. 2006b, hereafter R06).

Access to a third tracer of star formation, independent of the UV and IR emission, is required to establish a more secure footing for (1) the scaling between mid-IR emission and SFR and (2) the dependence of UV slope on dust extinction. The most direct probe of young massive star formation is from H II recombination nebular emission. In particular, the Hα line has been used traditionally as a SFR indicator given its accessibility in the optical window and the fact that it traces star formation on very short timescales ($\sim$10 Myr) and is less sensitive to extinction than UV emission (e.g., Kennicutt 1998; Brinchmann et al. 2004). Fortunately, Hα is still accessible with ground-based near-IR spectrographs for galaxies at $z \sim 2$. Using a sample of 114 UV-selected galaxies at $z \sim 2$ with Hα spectroscopy, Erb et al. (2006b) demonstrate that the Hα-inferred SFRs agree well with those obtained from the UV after correcting both the Hα line and the UV continuum magnitude for extinction, and assuming that $E(B-V)_{\rm stellar} \approx E(B-V)_{\rm nebular}$. In this paper, we use this Hα spectroscopic sample as the basis for quantifying independently the scaling between mid-IR emission and SFR for moderately luminous galaxies at $z \sim 2$. This scaling relation is then used to infer bolometric luminosities and dust obscuration and determine how the UV slope varies with extinction for typical high-redshift galaxies.

We begin by discussing in Section 2 the rest-UV selection, follow-up optical and near-IR spectroscopy, and the MIPS observations, data reduction, and photometry. The stellar population modeling of galaxies in our final samples is discussed in Section 3. We then present the correlations between Hα, X-ray, and 8 μm luminosity (and the connection between these quantities and the SFR) and comparison with other local and high-redshift relations (Section 4). The variation of UV slope with dust attenuation is addressed in Section 5. The correlation between bolometric luminosity and dust attenuation and the implications of this relationship for the observed UV luminosity are presented in Section 6. Finally, in Section 7 we present the results of a comparison between extinction and gas-phase metallicities of star-forming galaxies at $z \sim 2$ and demonstrate a close relationship between the two. We assume a Chabrier (2003) IMF unless stated otherwise and adopt a cosmology with $H_0 = 70$ km s^{-1} Mpc^{-1}, $\Omega_\Lambda = 0.7$, and $\Omega_{\rm m} = 0.3$.

2. SAMPLE

2.1. Optical and Hα Observations and Spectroscopy

The photometry and spectroscopic follow-ups for the Lyman break galaxy (LBG) survey at redshifts $1.4 \lesssim z \lesssim 3.4$ are described in Steidel et al. (2003), Steidel et al. (2004), and Adelberger et al. (2004). Briefly, galaxies were photometrically selected using either the "BM," "BX," or LBG rest-UV color criteria. A subset of $\mathcal{R} < 25.5$ candidates that were spectroscopically confirmed with Keck/LRIS observations (Steidel et al. 2004) were targeted with NIRSPEC H- or K-band spectroscopy to trace Hα (Erb et al. 2006c). In addition to the long-slit Hα spectroscopy, we targeted the $z = 2.300$ redshift overdensity in the HS1700+64 ("Q1700") field (Steidel et al. 2005) with narrowband Brγ (2.17 μm/0.04 μm) observations that trace Hα at that redshift. These images, along with $K_{\rm s}$-band observations, were obtained with the Wide-field Infrared Camera (WIRC) on the Palomar 5 m telescope. Details on the Brγ imaging reductions, continuum subtraction, and Hα flux determinations will be provided in a forthcoming paper (Steidel et al. 2010). Briefly, we calibrated the Brγ image by adjusting its zero point until the difference between $K_{\rm s}$ and Brγ magnitude was zero for objects of similar faintness in $K_{\rm s}$. Colors were measured in matched isophotal apertures with detection done at $K_{\rm s}$ band. We then measured the narrowband fluxes and subtracted the continuum based on the Brγ–$K_{\rm s}$ colors and knowledge of the Brγ filter bandwidth and shape. Photometric and zero-point uncertainties result in an $\simeq$20% error in the derived line fluxes.

This procedure resulted in 21 objects with $>5\sigma$ flux limits in Hα, ranging in flux from $\sim 5 \times 10^{-17}$ to $\sim 3 \times 10^{-16}$ erg s^{-1}. Eleven of these 21 objects also have long-slit Hα observations. Combining the long-slit and narrowband Hα samples yields a total number of 116 galaxies in six fields that have 24 μm coverage and are spectroscopically confirmed to lie at $1.5 \leqslant z \leqslant 2.6$, where the 24 μm data are sensitive to the rest-frame 8 μm flux (Section 2.3).

2.2. Correction for Slit Loss

The primary uncertainty in the spectroscopically derived Hα fluxes is slit loss. The overlap of 11 objects between the Hα long-slit and narrowband samples in the Q1700 field allows us to quantify this source of error. To assess the degree of [N II] contamination of the narrowband fluxes, we constructed a composite spectrum of the 11 objects with both long-slit and narrowband observations. From this composite, we determine a mean ratio of the [N II]-to-Hα flux of $\approx$0.09 for these 11 objects. At the redshift of these galaxies ($z = 2.300$), the Brγ transmission curve will suppress the [N II] line by a factor of 0.88 relative to Hα. Therefore, we expect the average [N II] line contamination of the narrowband flux to be $\approx$8%, translating to a 0.03 dex correction in log flux. After taking into account this 8% correction, the ratio of the narrowband Hα flux to the spectroscopic Hα flux for these 11 objects varies from 1.14 to 4.21, with a median value of 1.87 and a 1σ dispersion around this median value of $\sim$0.8 (i.e., a scatter of $\approx$40%). This median value is similar to the average slit loss correction factor of 2.0 suggested by Erb et al. (2006b). For galaxies with near-IR spectroscopic observations only, we correct the Hα flux for slit losses by multiplying by the median value found above, 1.87.

The sample of 11 galaxies with both long-slit and narrowband observations have an Hα flux distribution that is undistinguished from the distribution for the 90 galaxies that are used to measure the relation between 8 μm luminosity ($L_8 = \nu L_\nu(8\ \mu{\rm m})$) and L(Hα). Over this flux range, we find no dependence of the slit loss correction factor with the spectroscopic flux. The absence of any spectroscopic flux-dependent systematic in the slit loss correction, combined with the expectation that the amount of Hα flux lost in the spectroscopic observations depends sensitively on the relative placement and position angle of the slit on the galaxy, leads us to the conclusion that the slit loss correction must be dominated by random error.

2.3. MIPS Observations

There are six fields in the LBG survey that have *Spitzer* MIPS 24 μm coverage, including the publicly available data in the

GOODS-N and Westphal fields (M. Dickinson et al. 2010, in preparation; R. Chary et al. 2010, in preparation). We obtained observations in four additional LBG fields: Q1623, Q1700, Q2343, and Q1549 (see Reddy & Steidel 2009). Observations in these four fields consisted of 30 s frame times with two mapping cycles, where each cycle consists of a 3×3 dither pattern with a step size of 1/8 the size of the MIPS array. The total exposure time in 3 of the 4 fields is $\approx$11.4 hr, sufficient to detect $\approx$15 μJy sources at $>3\sigma$ (in the absence of confusion) within the inner $4'$ of each field. This is comparable to the depth of the 24 μm data in the GOODS-N and Westphal fields. The Q1700 MIPS data consist of $\approx$20 hr of observations and reach a 3σ depth of $\approx$10 μJy in the absence of confusion.

The 24 μm images are processed using a procedure similar to that described in R06. Briefly, the data are flat-fielded and then combined using MOPEX (Makovoz & Marleau 2005). Photometry is extracted using point-spread function (PSF) photometry with priors determined by the locations of objects detected in the IRAC images (IRAC data exist in all six fields). There are three sources of uncertainty in the 24 μm fluxes. The first is background noise, which we determine by fitting PSFs simultaneously to random positions around the target of interest and any other known sources. The dispersion in measurements of the background level obtained in this way is similar to the dispersion we would estimate by comparing the simulated and recovered fluxes of artificial objects added to the 24 μm images. The second source of uncertainty is Poisson error and is generally negligible compared to the background dispersion. The third source of uncertainty is confusion, which is reflected by the degeneracy between the PSF fit to the object of interest and the fits to any nearby sources. The uncertainty in the fit is computed simply from the covariance matrix for the N number of objects that are being fitted simultaneously. The total (normalized) covariance in the fit ($\sigma_{\rm cov}$) is a number between 0 and 1, where the former indicates no covariance with nearby objects and the latter indicates total covariance (e.g., such as the covariance between the fit of an object and itself). For most galaxies in the sample of 116, $\sigma_{\rm cov} \ll 1$. There are 17 out of 116 galaxies that have $\sigma_{\rm cov} > 0.3$. We consider these sources to be confused and remove them from our sample; this results in 99 galaxies with secure PSF fits.

2.4. Identification of AGN

Because we are interested primarily in the star-forming galaxies, we have removed active galactic nuclei (AGNs) from the sample based on (1) the presence of prominent emission lines including Lyα, C IV, and N V, or (2) an SED that behaves as a power law between rest-frame $\sim$2 μm and 8 μm (Section 3). Among the 99 unconfused galaxies in our sample, 9 are identified as AGN. Roughly half of these AGN also exhibited high ratios of [N II]/H$\alpha \gtrsim 0.5$. The fraction of AGN ($\approx$9%) is somewhat larger than the $\sim$5% found among typical LBGs to $\mathcal{R} = 25.5$ (Reddy et al. 2006a); the Hα spectroscopic sample is biased toward more K-bright galaxies relative to the typical LBG (Erb et al. 2006b), and the frequency of AGN increases rapidly with increasing K-band brightness at $z \sim 2$ (Reddy et al. 2005).

2.5. Final Samples

The sample used to measure the relationship between mid-IR luminosity and SFR consists of 90 galaxies in the Hα sample (including spectroscopic and narrowband-selected objects) that satisfy the following criteria: (1) $1.5 \leqslant z_{\rm spec} \leqslant 2.6$, (2) $\sigma_{\rm cov} < 0.3$, and (3) do not show AGN signatures based on optical emission lines or a power-law SED. Of these 90 galaxies, 29 are undetected at 24 μm to 3σ. We use a larger sample of 158 UV-selected galaxies in the GOODS-N field that satisfy the three criteria specified above and have corresponding X-ray data that allow us to perform an X-ray stacking analysis (Section 4.2). Finally, the relationship between dustiness and UV spectral slope is investigated with a sample of 392 galaxies (from 5 of the 6 LBG fields with MIPS data) that satisfy the three criteria above and have had their photometry modeled using a stellar population analysis (Section 3).

3. STELLAR POPULATION MODELING

To provide a broader context for interpreting the extinction properties, we have derived ages and stellar masses by modeling the broadband photometry of galaxies in our sample. All of the galaxies with MIPS data have been imaged with IRAC, enabling us to use the full rest-frame UV through near-IR photometry to fit for their stellar populations. Previous efforts in this regard are described in Shapley et al. (2005), Erb et al. (2006c), and Reddy et al. (2006a). Here, we update these results using the latest models of S. Charlot & G. Bruzual (2010, in preparation, hereafter CB10) that include the Marigo & Girardi (2007) prescription for the thermally pulsating asymptotic giant branch (TP-AGB) evolution of low- and intermediate-mass stars. The effect of this evolution on the inferred ages and stellar masses is then determined by comparing with our previous results that employed the Bruzual & Charlot (2003, hereafter BC03) models.

3.1. Modeling Procedure

For each galaxy, we considered a constant star formation (CSF) model and exponentially declining star formation histories with characteristic timescales $\tau = 10, 20, 50, 100, 200, 500, 1000, 2000$, and 5000 Myr. We further considered a range of ages spaced roughly logarithmically between 1 and 5000 Myr, excluding ages older than the age of the universe at the redshift of each galaxy. In addition, allowed ages were restricted to be longer than the dynamical timescale of $\simeq$70 Myr, as inferred from velocity dispersion and size measurements of $z \sim 2$ LBGs (Erb et al. 2006b; Law et al. 2007). Reddening is taken into account by employing the Calzetti extinction curve and allowing $E(B-V)$ to range between 0.0 and 0.6. In Section 5.3, we also consider the effects of adopting the SMC extinction curve on the model results for the youngest galaxies in our sample. The model SED at each τ and age combination is reddened, redshifted, and attenuated blueward of rest-frame 1216 Å for the opacity of the intergalactic medium (IGM) using the Madau (1995) prescription. The best-fit normalization of this model is determined by minimizing its χ^2 with respect to the observed $U_{\rm n}G\mathcal{R}+JK_{\rm s}$+IRAC (3.6–8.0 μm) photometry. This normalization then determines the SFR and stellar mass. The model (and normalization) that gives the lowest χ^2 is taken to be the best-fit SED. We note the inherent degeneracy in this type of modeling. Typically there are several best-fit models that may adequately describe the observed photometry, even when the redshift is fixed to the spectroscopic value, though there is generally less variation in stellar mass than in the other parameters (τ, age, $E(B-V)$) among these best-fit models (Shapley et al. 2005, 2001; Papovich et al. 2001; Sawicki & Yee 1998).

In the subsequent analysis, we have adopted the best-fit parameters obtained with a CSF model for several reasons.

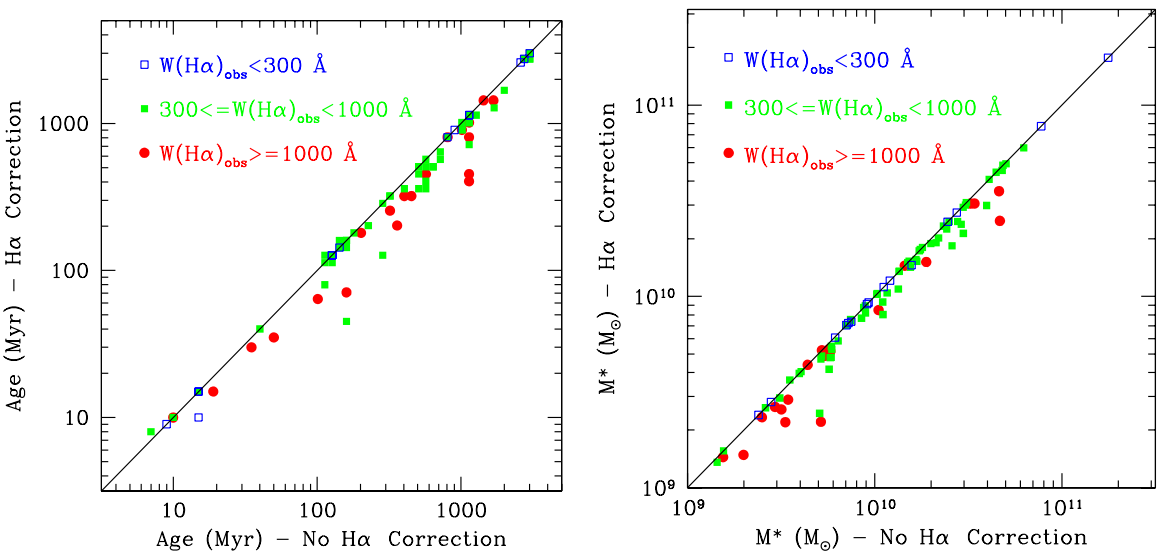

Figure 1. Comparison of the best-fit ages (left) and stellar masses (right) of 95 galaxies with Hα measurements before and after correcting the K_s-band flux for Hα line contamination. Points are color coded according to observed Hα equivalent width.

(A color version of this figure is available in the online journal.)

This model generally yields χ^2 values similar to those obtained when τ is allowed to vary freely. Additionally, some of the more extreme star formation histories are ruled out because the youngest galaxies in our sample cannot realistically have ages much less than the dynamical timescale of $\simeq$70 Myr. Such extreme models are also unlikely based on the presence of O star and Wolf–Rayet stellar features in the composite UV spectra of $z \sim 2$ galaxies, irrespective of age (e.g., Shapley et al. 2005). For simplicity, we do not consider more complex multi-component or stochastic star formation histories as the data would not allow for discrimination between them as compared to simpler star formation histories. Finally, we do not use the SFRs from the SED fitting in the subsequent analysis, opting instead to use the direct tracers examined here, including UV, Hα, X-ray, and 8 μm luminosity.

3.2. Effect of Hα Emission on the SEDs

The parameters of most interest are the age and stellar mass, both of which are determined primarily by the strength of the Balmer and 4000 Å breaks and the stellar continuum flux as traced by the near-IR and IRAC photometry at $z \sim 2$. Because the Hα emission line falls in the K_s band at $z \sim 2.0$–2.6, it is prudent to determine what effect, if any, the line has on biasing our estimates of the ages and stellar masses. Figure 1 summarizes the comparison of the best-fit ages and stellar masses (assuming CSF) obtained with and without correcting for the Hα contribution to the K_s-band flux for 95 galaxies with Hα measurements. Roughly two-thirds of the sample of 95 galaxies show no change in best-fit age or stellar mass after correcting the K_s-band flux for Hα line contamination, and not surprisingly these galaxies generally have small Hα equivalent widths ($W_{\rm obs} \lesssim 300$ Å). Even for those galaxies with larger Hα equivalent widths, the mean difference in age and stellar mass is relatively small compared to the uncertainty in these parameters as a result of the significant degeneracies inherent in SED fitting.

The small differences in the ages and stellar masses before and after correcting for Hα emission partly reflect the fact that these parameters are not solely constrained by the near-IR data: 89 of the 95 galaxies also have higher signal-to-noise ratio (S/N) IRAC data that are unaffected by line contamination at these redshifts. Also note that the age distribution for galaxies with the largest Hα equivalent widths ($W_{\rm obs} \gtrsim 1000$ Å), including many of those selected from the narrowband data of the Q1700 field (Section 2), is not significantly different from that of galaxies with smaller equivalent widths. The lack of a significant trend between Hα equivalent width and age for this sample has been noted by Erb et al. (2006b), and may be due to the stochasticity of the instantaneous SFR. In any case, given that the age and SFR distribution of galaxies with Hα measurements span roughly the entire range probed by UV-selected galaxies in general (Erb et al. 2006c), and that the correction for the Hα flux does not significantly alter the best-fit ages and stellar masses for the majority of the sample, we are confident in our ability to constrain the SED fits of galaxies at $z \sim 2.0$–2.6 even in the absence of direct measurements of the Hα line contamination in the K_s band.

3.3. Comparison between CB10 and BC03

Figure 2 compares the BC03 and CB10 derived stellar masses for 1156 UV-selected galaxies with spectroscopic redshifts $1.40 < z < 3.50$, color coded by the BC03-derived stellar age. The TP-AGB phase will become important $\simeq$200 Myr after the onset of star formation. Anywhere from 50% to 60% of galaxies older than this have CB10 derived stellar masses that deviate by more than 20% from their BC03-derived stellar mass, with a median CB10 stellar mass that is a factor of $\sim$1.5 times lower than the BC03 stellar mass. The CB10 models also imply ages that are on average 100 Myr younger than BC03-derived ages. We will make use of the CB10 derived ages, stellar masses, and color excesses in the subsequent analysis.

4. DEPENDENCE OF 8 μm LUMINOSITY ON STAR FORMATION RATE

4.1. Computing the Mid-IR and Hα Luminosities

The 8 μm luminosity, L_8, is computed by k-correcting the 24 μm flux using the average mid-IR spectral shape of local starburst galaxies, as discussed in R06. All 90 galaxies

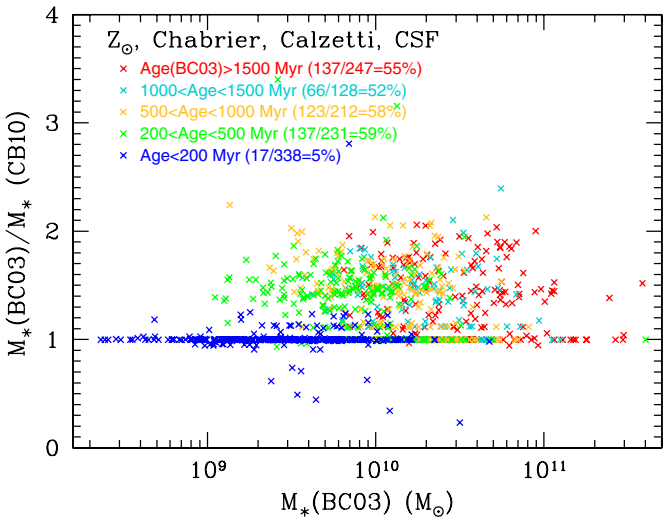

Figure 2. Ratio of BC03 to CB10 derived stellar masses as a function of BC03-derived stellar mass for 1156 UV-selected galaxies with spectroscopic redshifts $1.40 < z < 3.50$. Fractions indicate the percentage of objects in each age range that have CB10 masses that deviate more than 20% from the BC03 mass.

(A color version of this figure is available in the online journal.)

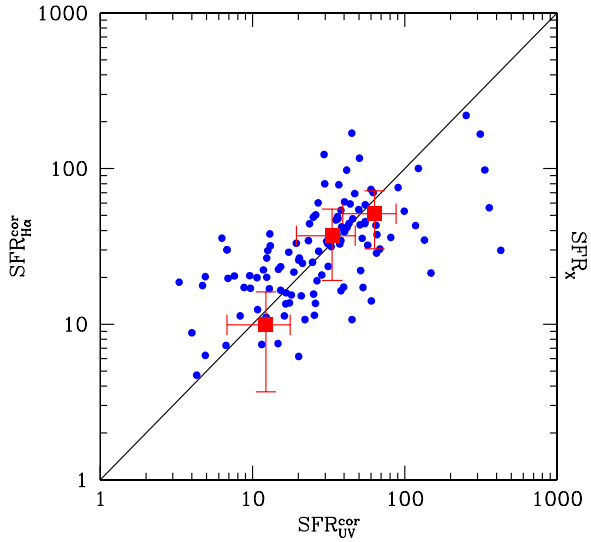

Figure 3. Dust-corrected Hα SFR vs. UV SFR (blue symbols; data from Erb et al. 2006b) compared to X-ray determined SFRs (red symbols).

(A color version of this figure is available in the online journal.)

have *spectroscopic* redshifts and therefore are immune to the additional 0.3 dex uncertainty introduced by photometric redshift errors typical of $z \sim 2$ star-forming galaxies, owing to the complicated mid-IR spectral shape and the redshift sensitivity of the *k*-correction (R06).

Hα luminosities are corrected for extinction based on the $E(B-V)$ color excess as derived from the SED fitting (Section 3). The average color excess is $\langle E(B-V)\rangle = 0.15 \pm 0.10$, implying an average UV attenuation of a factor of ∼4–5 (Reddy & Steidel 2004; Reddy et al. 2006b). Similar average dust obscurations have been obtained based on stacked X-ray analyses of LBGs at $z \sim 3$ (e.g., Seibert et al. 2002; Nandra et al. 2002; Reddy & Steidel 2004). Adopting the conversion $E(B-V)_{\rm stellar} = 0.4E(B-V)_{\rm nebular}$ advocated by Calzetti et al. (2000) results in Hα-inferred SFRs that notably overpredict those derived from the X-ray and dust-corrected UV for the sample presented here (Erb et al. 2006b). Therefore, the same value of $E(B-V)$ is assumed for both the UV continuum and nebular emission lines.[9] The Calzetti et al. (2000) extinction curve then implies a mean Hα extinction correction of 1.71 ± 0.40. The uncertainty in the observed Hα luminosity is dominated by random error in the slit loss correction factor and is taken to be ≈40% (Section 2.2).

[9] Förster Schreiber et al. (2009) find evidence in their sample of $z \sim 2$ galaxies targeted with *VLT*/SINFONI observations that the extinction of the nebular regions may be larger than that for the stellar continuum, though their sample includes galaxies with somewhat larger SFRs and larger stellar masses than those typical of galaxies in our sample. It is possible that the nebular reddening may on average be larger for galaxies that are forming stars at a higher rate and/or hosting an older (less attenuated) stellar population (e.g., Epinat et al. 2009). While we note that some small amount of additional nebular extinction may be allowable by our data after correcting for slit losses (given the ≈40% random scatter in such losses), this systematic difference in attenuation is likely to be small relative to the scatter in the slit loss correction and the scatter in correlation between dust-corrected Hα and dust-corrected UV SFRs of ≈0.3 dex. Given that the galaxies (with Hα observations) analyzed here are drawn from the same sample presented in Erb et al. (2006b), and the fact that these authors found no significant evidence for a larger obscuration toward the nebular regions in these galaxies, we proceed under the assumption that $E(B-V)_{\rm stellar} = E(B-V)_{\rm nebular}$.

4.2. X-ray Stacking Analysis

Recall that our main goal is to determine how mid-IR luminosity scales with SFR by cross-correlating the *Spitzer* data with dust-corrected Hα luminosity. We have two independent measures of how well the dust-corrected Hα luminosity scales with SFR. For instance, Erb et al. (2006b) and Reddy & Steidel (2004) demonstrate the agreement between dust-corrected UV, dust-corrected Hα, and stacked X-ray estimates of the SFRs of the same types of galaxies at $z \sim 2$ that are examined in this study. To provide better constraints, and to take advantage of the new spectroscopy done after these initial studies, we revisited the use of X-ray emission as a proxy for SFR in our larger UV spectroscopic sample. To accomplish this, we made several stacks of the deep *Chandra* 2 Ms X-ray data in the GOODS-North field (Alexander et al. 2003) for galaxies in both the Hα and larger UV samples, restricting the analysis to those galaxies with spectroscopic redshifts. The X-ray stacking analysis is performed in a manner identical to that specified in Reddy & Steidel (2004). The errors on the Hα and UV luminosities and SFRs reflect the object-to-object dispersion in Hα/UV luminosity among the stacked galaxies. Examination of both the mean and median stacks of the X-ray data suggests that there are no galaxies that dominate the X-ray signal and bias the mean stacked results. The results of the stacking analysis are summarized in Table 1, along with conversions to SFRs listed in Table 2. We will refer to these results throughout the paper. For the time being, we point out that the SFRs inferred from X-ray emission are broadly consistent with those derived from both the UV and Hα emission once the latter two are corrected for dust assuming the Calzetti extinction curve. Consequently, the mean dust correction derived using the Calzetti prescription is similar to the mean dust correction obtained by comparing the X-ray SFRs with those derived from the observed UV and Hα SFRs, even when restricting the sample to those galaxies within a specific range of SFR (Figure 3). We will revisit the correlation between UV slope and dust attenuation in Section 5. Based on the agreement between X-ray and dust-corrected Hα and UV inferences of the SFRs, we adopt the dust-corrected Hα luminosity as a proxy for the bolometric SFR.

Table 1
Stacked X-ray and Hα and UV Luminosities

Sample (1)	N[a] (2)	$F_{0.5-2.0\,keV}$[b] (3)	$L_{2.0-10.0\,keV}$[c] (4)	$L_{H\alpha}^{obs}$[d] (5)	$L_{H\alpha}^{cor}$[e] (6)	L_{UV}^{obs}[f] (7)	L_{UV}^{cor}[g] (8)
Hα (All)	18	6.6 ± 2.4	3.4 ± 1.3	4.3 ± 2.6	7.4 ± 4.4	11.5 ± 6.3	54.4 ± 30.0
Hα (Undet)[h]	8	3.3 ± 1.5	1.8 ± 0.8	3.5 ± 2.2	4.9 ± 3.1	12.2 ± 5.9	32.4 ± 15.8
UV (All)	158	5.1 ± 1.8	1.8 ± 0.6	...	...	7.6 ± 4.1	41.0 ± 22.3
UV (Undet)[h]	116	2.8 ± 1.7	1.0 ± 0.6	...	...	7.4 ± 3.9	29.3 ± 15.4
UV (0 < SFR < 20)[i]	58	2.4 ± 1.5	0.9 ± 0.6	...	...	5.9 ± 2.6	15.7 ± 7.0
UV (20 < SFR < 40)[i]	43	9.6 ± 4.6	3.3 ± 1.6	...	...	7.9 ± 3.3	42.9 ± 17.9
UV (40 < SFR < 80)[i]	32	12.2 ± 5.0	4.6 ± 1.9	...	...	8.4 ± 5.3	81.4 ± 31.1
UV (0 < SFR < 20; Undet)[h,i]	56	2.0 ± 1.7	0.7 ± 0.6	...	...	5.9 ± 2.7	15.7 ± 7.1
UV (20 < SFR < 40; Undet)[h,i]	28	5.8 ± 3.1	2.3 ± 1.2	...	...	8.7 ± 3.5	46.9 ± 18.7
UV (40 < SFR < 80; Undet)[h,i]	16	8.4 ± 4.4	3.9 ± 2.1	...	...	8.9 ± 5.6	78.2 ± 29.5

Notes.
[a] Number of galaxies in sample.
[b] Average soft-band X-ray flux, in units of 10^{-18} erg s^{-1} cm^{-2}.
[c] Average X-ray luminosity in units of 10^{41} erg s^{-1}, assuming an X-ray photon index of $\Gamma = 2.0$ and Galactic absorption column density of 1.6×10^{20} cm^{-2} (Stark et al. 1992).
[d] Observed Hα luminosity in units of 10^{42} erg s^{-1}, uncorrected for dust.
[e] Dust-corrected Hα luminosity in units of 10^{42} erg s^{-1}.
[f] Observed UV luminosity in units of 10^{28} erg s^{-1} Hz^{-1}, uncorrected for dust.
[g] Dust-corrected UV luminosity in units of 10^{28} erg s^{-1} Hz^{-1}.
[h] Stack of galaxies not detected at 24 μm.
[i] Stack of galaxies with dust-corrected UV-inferred SFRs in $M_\odot$ yr^{-1} as specified, assuming a Chabrier IMF.

Table 2
Star Formation Rates and Attenuation from X-ray, Hα, and UV

Sample[a] (1)	SFR_X[b] (2)	$SFR_{H\alpha}^{obs}$[b] (3)	$SFR_{H\alpha}^{cor}$[b] (4)	$A_{H\alpha}^{E(B-V)}$[c] (5)	$A_{H\alpha}^{X-ray}$[d] (6)	SFR_{UV}^{obs}[b] (7)	SFR_{UV}^{cor}[b] (8)	$A_{UV}^{E(B-V)}$[c] (9)	A_{UV}^{X-ray}[d] (10)
Hα (All)	37 ± 14	19 ± 11	32 ± 19	∼1.7	∼1.9	9 ± 5	42 ± 23	∼4.7	∼4.1
Hα (Undet)	20 ± 9	15 ± 10	22 ± 13	∼1.5	∼1.3	9 ± 5	25 ± 12	∼2.8	∼2.2
UV (All)	20 ± 7	...	...	...	...	6 ± 3	32 ± 17	∼5.3	∼3.3
UV (Undet)	12 ± 7	...	...	...	...	6 ± 3	23 ± 12	∼3.8	∼2.0
UV (0 < SFR < 20)	10 ± 6	...	...	...	...	5 ± 2	12 ± 5	∼2.4	∼2.0
UV (20 < SFR < 40)	37 ± 18	...	...	...	...	6 ± 3	33 ± 14	∼5.5	∼6.2
UV (40 < SFR < 80)	51 ± 21	...	...	...	...	7 ± 4	63 ± 24	∼9.0	∼7.3
UV (0 < SFR < 20; Undet)	8 ± 7	...	...	...	...	5 ± 2	12 ± 6	∼2.4	∼1.6
UV (20 < SFR < 40; Undet)	25 ± 13	...	...	...	...	7 ± 3	36 ± 15	∼5.1	∼3.6
UV (40 < SFR < 80; Undet)	44 ± 23	...	...	...	...	7 ± 4	61 ± 23	∼8.7	∼6.3

Notes.
[a] Samples are the same as in Table 1.
[b] In $M_\odot$ yr^{-1}, assuming a Chabrier IMF, based on the conversion relations of Ranalli et al. (2003) and Kennicutt (1998).
[c] Attenuation factor corresponding to $E(B-V)$ assuming the Calzetti et al. (2000) relation.
[d] Attenuation factor from the ratio of the X-ray-inferred SFR to the observed Hα and UV SFRs.

4.3. Correlation Between Hα and 8 μm Luminosity

Figure 4 shows L_8 versus dust-corrected Hα luminosity for the 90 galaxies in our sample.[10] Focusing on the 61 detected galaxies, we find a probability $P \simeq 0.00001$ that the L_8 and Hα luminosities are uncorrelated, implying a 4.4σ significance of the correlation. A linear fit to the data yields a slope consistent with unity and rms dispersion of 0.23 dex. In principle, stacking the 24 μm data for the 24 μm-undetected galaxies should provide additional constraints for them. However, unlike the Poisson-limited X-ray data, there are additional difficulties with stacking 24 μm data. The first is that the MIPS observations are typically background limited, requiring larger samples for a reliable stack. The second is that owing to the beam size of the MIPS observations, we must ensure that we include only well-isolated galaxies in the stack to avoid contamination from nearby galaxies, irrespective of whether the contaminants are detected at 24 μm. Unfortunately, there are not enough well-isolated 24 μm-undetected galaxies to obtain a reliable estimate of their stacked flux. Of the 29 undetected galaxies, 16 are at least 3″ away from any IRAC sources. Stacking the data for these 16 galaxies results in an upper limit only to their median 8 μm luminosity (Figure 4). In spite of these difficulties, we can use a survival analysis to take advantage of the censored data (upper limits in L_8) for the undetected galaxies to make a more robust measurement of the overall correlation between Hα and mid-IR luminosity.

There are several well-documented statistical techniques available for performing linear regression in the presence of censored data, including the Buckley–James (BJ) and expectation-

[10] For simplicity, we did not consider the small fraction (≈15%) of objects at $z \simeq 2.0$–2.6 targeted with NIRSPEC that did not yield Hα detections. Roughly half of the galaxies with Hα nondetections are also undetected at 24 μm. Including these in our analysis does little to alter the correlation between L_8 and dust-corrected Hα luminosity. Most of the remaining Hα nondetected sources had inaccurate astrometry which may have contributed to the lack of detection.

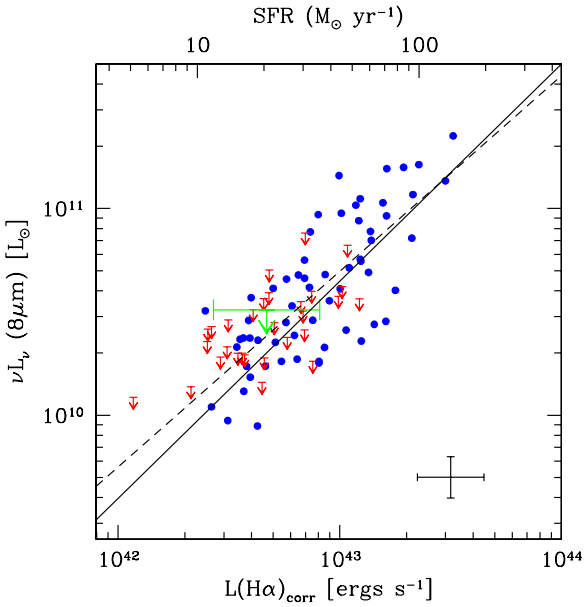

Figure 4. 8 μm vs. dust-corrected Hα luminosity for the 90 galaxies with both 24 μm observations and either long-slit or narrowband measurements of the Hα flux. The best-fit linear relation for the 61 detected objects (circles) is shown by the dashed line. The solid line shows the fit for all galaxies, including the 29 undetected galaxies (downward-pointing arrows). A stack of the 24 μm data for 16 well-isolated undetected galaxies yields a 3σ upper limit (large arrow), which is measured from the background dispersion in the stacked image. The width of the upper limit is determined from the dispersion of Hα luminosities of these 16 galaxies. The typical error on individual points is indicated in the panel.

(A color version of this figure is available in the online journal.)

maximization (EM) algorithms, both of which are implemented in the ASURV statistical software package (Isobe et al. 1986). Survival analysis assumes that the presence of an upper limit in a parameter (e.g., flux) is independent of the true value of the quantity being correlated (e.g., luminosity). This is usually satisfied in flux-limited surveys where the fundamental parameter is luminosity. Moreover, in our case, the 8 μm luminosities depend on distance in a highly nonlinear way because of the strong redshift dependence of the k-correction. Finally, the upper limits are determined by the depths of the 24 μm images which are independent of the luminosity distribution (i.e., we did not integrate for a longer period of time on fainter objects). Therefore, we assume that the 24 μm upper limits are roughly randomized with respect to the underlying 8 μm luminosity distribution.

In the EM algorithm, an initial guess is made for L_8 for the 24 μm-undetected galaxies based on the sample of detections and assuming a normal distribution of residuals about the linear fit. These guesses are then combined with the detected sample to produce a new linear fit between 8 μm and Hα luminosity. This new fit is then used to revise the initial guesses for the luminosities of the undetected galaxies, and the procedure is repeated until convergence. The BJ method works in a similar way, but makes no assumption for the distribution of points around the regression line, instead employing the Kaplan–Meier distribution derived from the sample (e.g., the 24 μm detection probability as a function of Hα luminosity). Both methods were used to quantify the relation between L(Hα) and L_8 using information for all 90 galaxies, and both methods yielded similar results. Including both the detections and nondetections, we find a probability $P \simeq 0.00001$ that L_8 and L(Hα) are uncorrelated, implying a 4.4σ significance of the correlation. A linear fit to the data yields an rms dispersion of 0.24 dex:

$$\log[L_8/L_\odot] = (1.05 \pm 0.11) \times \log[L(\mathrm{H}\alpha)/\mathrm{erg\,s^{-1}}] - (34.48 \pm 4.26) \quad \text{for } 10^{42} \lesssim L(\mathrm{H}\alpha) \lesssim 4 \times 10^{43}\ \mathrm{erg\,s^{-1}}. \tag{1}$$

Within the errors of the fitted parameters, the linear regressions with and without incorporating the upper limits are identical over the range of luminosity considered here. Note that the correlation between L_8 and dust-corrected L(Hα) is not solely due to any systematic change in the extinction correction with L_8 because we still find a significant 4.0σ correlation between L_8 and observed L(Hα) (uncorrected for extinction).

Aside from the statistical analysis, it is worth examining further how the 24 μm-undetected galaxies affect the overall fit between L_8 and L(Hα) based on physical grounds. We discussed already the limitations in stacking the 24 μm data for these galaxies. Therefore, we took advantage of the X-ray data for 24 μm-undetected galaxies in the GOODS-N field. An X-ray stack points to an average SFR of $\sim 20 \pm 9\ M_\odot\ \mathrm{yr}^{-1}$, very similar to that derived from the dust-corrected Hα (Table 2). Examination of the mean attenuation factors suggests also that while such 24 μm-undetected galaxies are less dusty than the detected galaxies—as expected from the fact that 24 μm emission traces the dust emission in galaxies—the former are not completely dust free given their relatively large SFRs and mean attenuation of $\sim$1.3–1.5. Hence, the undetected galaxies *cannot* have true mid-IR luminosities that fall substantially and systematically below the correlation defined in Equation (1), and therefore they must be described adequately by this correlation.

Combining the linear fit of Equation (1) with the relation between SFR and Hα luminosity (Kennicutt 1998), which assumes solar metallicity and does not include the effects of stellar rotation (e.g., Leitherer 2008), we obtain the following:

$$\log[\mathrm{SFR}/M_\odot\ \mathrm{yr}^{-1}] = (0.95 \pm 0.10) \times \log[L_8/L_\odot] - (8.52 \pm 0.87) \quad \text{for } 4 \times 10^9 \lesssim L_8 \lesssim 2 \times 10^{11}\ L_\odot. \tag{2}$$

The SFR in Equation (2) is a *total* dust-corrected SFR. In order to relate the mid-IR luminosity to total (8–1000 μm) infrared luminosity, $L_{\rm IR}$, we cannot simply combine Equation (2) with the Kennicutt relation between $L_{\rm IR}$ and SFR. This is due to the fact that the latter is derived under the optically thick limit in which a vast majority of the bolometric luminosity is obscured and emerges in the IR. While this is true for most of the galaxies in our sample, it will not be the case for fainter ones (e.g., such as those undetected at 24 μm) where a large fraction of the luminosity may be unobscured (Section 6). The dust-corrected Hα-inferred SFR is equivalent to the sum of the obscured (IR) and unobscured, or observed, (UV) SFRs. Therefore, we subtracted the observed UV SFR from the dust-corrected Hα SFR to determine the obscured SFR and IR luminosity. Taking the observed UV component of the SFRs into account, we arrive at the following relation between L_8 and $L_{\rm IR}$:

$$\log[L_{\rm IR}/L_\odot] = (1.37 \pm 0.16) \times \log[L_8/L_\odot] - (3.01 \pm 1.34) \quad \text{for } 4 \times 10^9\ L_\odot \lesssim L_8 \lesssim 2 \times 10^{11}\ L_\odot. \tag{3}$$

The importance of the correction for the unobscured SFR is illustrated in Figure 5 where we compare Equation (3) with that obtained assuming optically thick star formation. Galaxies with large 8 μm dust luminosities have a smaller fraction of their luminosity escaping in the UV, thus Equation (3)

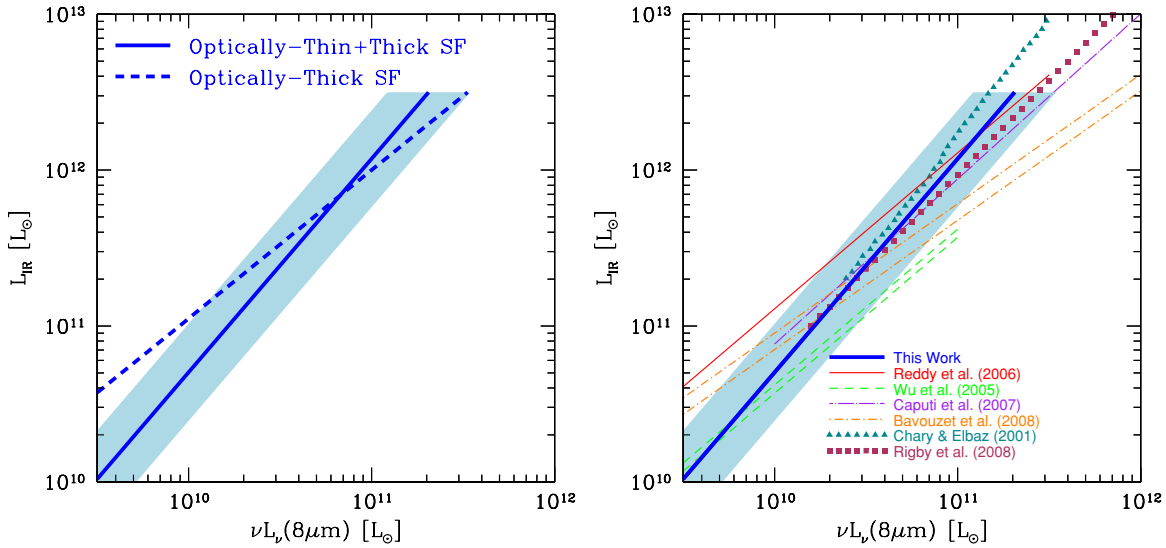

Figure 5. Left: comparison between L_{IR}–L_8 relations in the optically thick case and in the case where the emission is both optically thin and thick. L_{IR} is computed by subtracting the observed UV-derived SFR from the dust-corrected Hα SFR (see the text). Right: comparison of several published calibrations between L_8 and L_{IR}, with most data taken from Caputi et al. (2007), including those of Reddy et al. (2006b), Wu et al. (2005), Caputi et al. (2007), Bavouzet et al. (2008), Chary & Elbaz (2001), and Rigby et al. (2008). The calibration and rms (random) dispersion derived in our work are denoted by the thick blue line and shaded light blue region. We have plotted these relations over only the approximate luminosity range for which they are calibrated.

(A color version of this figure is available in the online journal.)

approaches what we would expect in the case where all of the star formation is optically thick. Alternatively, galaxies with small dust luminosities have a substantial fraction of luminosity emergent in the UV. In this case, the obscured SFR is lower than what we would have guessed in the optically thick case. The result is that the correlation between L_8 and L_{IR} predicts a factor of 4 lower L_{IR} than the optically thick case at $L_8 \sim 3 \times 10^9\ L_\odot$.

The equations above summarize the relationship between mid-IR luminosity, infrared luminosity, and total SFR over the ranges specified above, as derived from the correlation between 8 μm and Hα luminosity.

4.4. Comparison with Other High-redshift and Local Correlations

Figure 5 summarizes several published determinations of the relationship between L_8 and L_{IR}, compared with our determination at $z \sim 2$ (Equation (3)). There is a general agreement to a factor of ≈2 between the conversions over the luminosity range where they overlap ($10^{11}\ L_\odot \lesssim L_{IR} \lesssim 10^{12}\ L_\odot$). Excepting our present determination and that of Rigby et al. (2008), all the relations shown in Figure 5 were calibrated on galaxies at $z < 0.7$.[11] The calibration presented by Caputi et al. (2007) is in rough agreement with our relationship within the rms dispersion of the latter. The Wu et al. (2005) relations are calibrated on radio and Hα data for local galaxies ($z < 0.2$) drawn from the *Spitzer* First Look Survey (FLS; e.g., Frayer et al. 2006). Finally, the R06 calibration is derived based on the median L_8 to L_{IR} ratio of local galaxies in the Elbaz et al. (2002) sample. Focusing on the relations calibrated with $z \sim 2$ data, Rigby et al. (2008) report on the correlation between L_8 and L_{IR} based partly on a sample of four lensed galaxies with intrinsic L_{IR} between 10^{11} and $10^{12}\ L_\odot$. Their best-fit relation agrees broadly with ours over the luminosity range where the two are calibrated. The value of our analysis is that it incorporates the largest sample of its kind with Hα, UV, X-ray, and 24 μm observations of *spectroscopically* confirmed typical galaxies at $z \sim 2$. We proceed by adopting Equations (1)–(3).

5. RELATIONSHIP BETWEEN REST-FRAME UV SLOPE AND DUST ATTENUATION

While the previously derived calibrations are useful, most high-redshift galaxies are too faint or lie at too high redshift to be detected directly at 24 μm, thus suggesting the need for some other proxy for dust extinction. Meurer et al. (1999) demonstrated a tight correlation between dust attenuation and rest-frame UV slope, β, for a sample of nearby starburst galaxies. An advantage of using the UV slope as a proxy for dust obscuration is the ability to quantify it for galaxies that are up to 2 orders of magnitude fainter in bolometric luminosity, yet are several thousand times more numerous, than the dustiest ultraluminous galaxies (ULIRGs) at high redshift. Thus, it enables us to quantify the contribution of such galaxies to the bolometric luminosity density (e.g., Reddy et al. 2008; Reddy & Steidel 2009). The Meurer relation is widely used to recover the dust attenuation and bolometric luminosities of high-redshift galaxies; however, its validity had not been tested directly for such galaxies until recently. Based on a UV-selected sample of spectroscopically confirmed 24 μm detected galaxies and stacked X-ray analysis in the GOODS-N field, R06 demonstrated that the local relation appears to hold for galaxies with bolometric luminosities (sum of the IR and UV luminosities) between 10^{11} and $10^{12.3}\ L_\odot$ at $z \sim 2$, luminosities typical of L^* galaxies at these redshifts. Here, we re-evaluate the sensitivity of β to dust attenuation using the full UV-selected sample of 392 galaxies with 24 μm data and SED modeling.

In the subsequent discussion the dust attenuation, IRX, is parameterized by the ratio of the infrared luminosity (computed using Equation (3)) to UV luminosity (uncorrected for dust). The intrinsic UV spectral slope β is determined from the $G - \mathcal{R}$

[11] Bavouzet et al. (2008) test the validity of their results for higher redshift galaxies by comparing with stacked 24, 70, and 160 μm measurements (from the three MIPS bands) for galaxies at $z \approx 1.7$, and they find a mean L_8 to L_{IR} ratio similar to that of $z < 0.7$ galaxies. Both of their fits with and without the stacked data are shown in Figure 5.

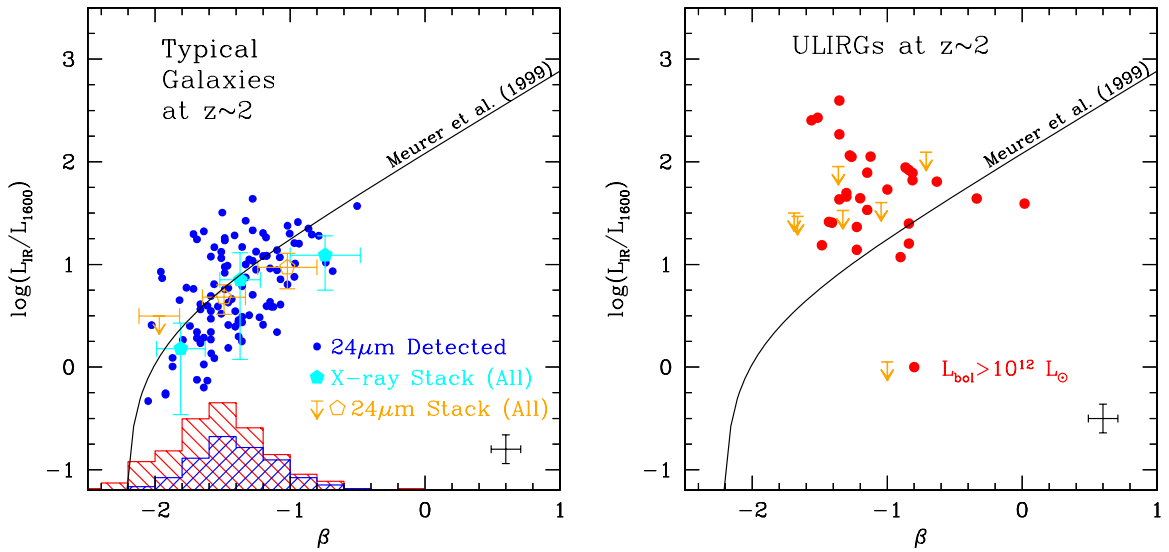

Figure 6. Left: dust attenuation, parameterized as the ratio between infrared and UV luminosity, vs. rest-frame UV slope, β, for typical galaxies at $z \sim 2$ (see the text). The typical error in the 24 μm detected points is indicated at the lower right. The filled pentagons show our inferences from stacked X-ray data, where the error bars reflect the 1σ dispersion in the relevant quantity for the stacked galaxies, which is typically larger than the formal uncertainty in the stacked X-ray flux. Similarly, the upper limit and open pentagons denote results from the 24 μm stacks. The arbitrarily normalized red and blue histograms show the β distribution for galaxies undetected and detected, respectively, at 24 μm. Right: same as left panel for bolometrically luminous galaxies (ULIRGs). Upper limits are shown for 24 μm-undetected galaxies.

(A color version of this figure is available in the online journal.)

color as follows. We generated power laws in $f(\lambda) \propto \lambda^{\beta}$ for $-2.5 \leqslant \beta \leqslant 1.0$ with $\Delta\beta = 0.01$. These are attenuated for the Lyα forest opacity assuming the Madau (1995) prescription and multiplied by the G and $\mathcal{R}$ transmission filters. The UV slope is taken to be the one which gives a $G - \mathcal{R}$ color closest to the observed value. In the present analysis, β is simply an observed quantity and is immune to the uncertainties associated with SED fitting (e.g., as would be the case with a SED-derived value of $E(B-V)$). The error in UV slope is related directly to the error in color, and is typically $\sigma_{\beta} \simeq 0.11$.[12]

5.1. Results for Typical Star-forming Galaxies at $z \sim 2$

To aid our discussion, we focus first on the correlation between UV slope and attenuation for typical star-forming galaxies at $z \sim 2$, which we define formally as those galaxies with bolometric luminosities, $L_{\rm bol} = L_{\rm IR} + L_{\rm UV} < 10^{12}\ L_{\odot}$, and ages older than 100 Myr as determined from the broadband SED fitting. These limits are adopted to reflect the characteristics of the vast majority of star-forming galaxies at $z \sim 2$. Constraints on the bolometric luminosity function imply that a typical galaxy at $z \sim 2$ will have a characteristic luminosity $L^{*}_{\rm bol} \sim 2 \times 10^{11}\ L_{\odot}$ (Reddy et al. 2008). Further, our SED modeling implies a median age of 360 Myr with a dispersion of ≈810 Myr, where ≈13% have ages younger than 100 Myr. There are 311 galaxies that under this definition are classified as "typical," and 109 of these (35%) are detected at 24 μm. These detected galaxies exhibit UV slopes that are correlated with attenuation (3.8σ significance) with a formal scatter of 0.38 dex about a linear fit (Figure 6). The normalization of this correlation will depend of course on the depth of the 24 μm data, as we might expect that the detected galaxies have dust attenuations that are larger than those for undetected galaxies for a fixed β. For a fairer representation that is robust to the mid-IR observational depth limitations, we have stacked the X-ray data for galaxies in the GOODS-N field in three bins of β, irrespective of whether they are detected at 24 μm. We convert the mean X-ray determined SFR to an IR luminosity after taking into account the fraction of light emerging in the UV (see discussion in Section 4.3), and we find mean attenuation factors that exhibit the same trend with β as the 24 μm-detected galaxies (Figure 6). These results are in broad agreement with those obtained by stacking the 24 μm data in bins of β.

More generally, the mid-IR nondetections exhibit a β distribution that is statistically unlikely to be drawn from the same parent distribution as the mid-IR detected galaxies. A two-sided K–S test indicates a probability of 0.01 that the distribution in β for 24 μm detections is drawn from the same distribution as that for the 24 μm-undetected galaxies. While both samples include galaxies over approximately the full range of β, those that are undetected at 24 μm have UV slopes that are systematically bluer on average by $\Delta\beta \sim -0.1$ than the detected ones.

The IRX–β trend combined with our observations of the β distributions for the detected versus undetected galaxies implies then that the 24 μm-undetected galaxies are on average less dusty than the detected galaxies, in accord with expectations. Further, we find that the 24 μm detection fraction increases steadily with β for typical star-forming galaxies, implying that galaxies with redder spectral slopes are on average more infrared luminous (Figure 7). In the next section, we show that the relationship between β and luminosity fails for the most luminous galaxies at $z \sim 2$.

The correlation between attenuation and UV slope for typical L^{*} galaxies at $z \sim 2$ is not necessarily surprising considering our expectations given the correlation between mid-IR luminosity and the Hα luminosity corrected for dust based on the UV slope (Figure 4). Perhaps more importantly, the IRX–β relation at $z \sim 2$ is indistinguishable from that established for local UV-starburst galaxies (Meurer et al. 1999), the same relation that

[12] The G band is affected by the Lyα forest only for redshifts $z \gtrsim 2.5$. Therefore, statistical fluctuations in the forest will not affect our determination of β as most of the galaxies in the samples considered here are at $z \lesssim 2.5$. For the same reason, Lyα contamination of the G-band flux is not a concern in our determination of β.

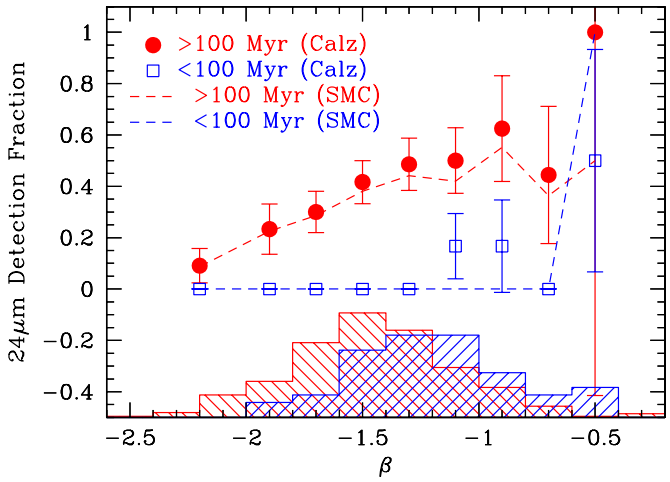

Figure 7. 24 μm detection fraction as a function of UV spectral slope β for typical galaxies with ages >100 Myr and young galaxies with ages $\lesssim$100 Myr in the case of ages derived assuming a Calzetti extinction curve (open squares and solid circles). Errors assume Poisson statistics. The dashed lines show the same when we assume an SMC extinction curve in deriving the ages. The histograms show the arbitrarily normalized β distributions (in the case of Calzetti-derived ages) for the two subsamples, and a two-sided K–S test indicates a probability $P \lesssim 0.01$ that the two are drawn from the same parent distribution (see the text).

(A color version of this figure is available in the online journal.)

is almost always used to determine dust-corrected luminosities at high redshift.[13] This agreement has been noted previously for galaxies selected using other techniques (e.g., the BzK-selected sample of Daddi et al. 2007) as well as UV-selected spectroscopic samples of L^* galaxies at $z \sim 2$ (R06; Adelberger & Steidel 2000). Further, the SFRs derived by correcting the observed UV luminosity for dust using the Meurer relation agree well with the SFRs inferred from the SED fitting (left panel of Figure 8). This result is of course not surprising since the Calzetti extinction curve (which is essentially coincident with the Meurer relation) is used in the SED fitting to estimate reddening and SFRs, both of which are driven primarily by the UV slope. The practical utility demonstrated here is that the UV slope can be used to recover the dust attenuation of typical high-redshift star-forming galaxies to within a 1σ scatter of $\approx$0.4 dex. This strengthens our confidence in using the Meurer relation to recover dust attenuation from the UV SED of L^* galaxies in the absence of longer wavelength data.

5.2. Bolometrically Luminous Galaxies

Turning now to bolometrically luminous galaxies with $L_{\rm bol} > 10^{12}\ L_\odot$, we find that they have systematically larger IRX ratios than we would have inferred from the Meurer relation. This bias is roughly 4–5 times larger than the random error in the IRX ratio and is generally attributed to the fact that significant amounts of star formation are completely obscured in the UV (e.g., Reddy et al. 2006b; Papovich et al. 2006; Chapman et al. 2005; Goldader et al. 2002). Hence, the reddening deduced from the UV SED tends to be lower than that inferred from more direct tracers of the obscured star formation.

A pertinent question to address is whether our conversion from 24 μm flux to infrared luminosity is applicable for such luminous galaxies because, as the reader will recall, our calibration is based primarily on galaxies with $L_{\rm bol} \lesssim 10^{12}\ L_\odot$. An examination of the empirically derived fits shown in Figure 5 illustrates that, with the exception of the Bavouzet relation, our estimate of $L_{\rm IR}$ for these luminous objects is similar to what we would have predicted from the other relations. Adopting the Bavouzet prediction would lower the IRX ratio by $\approx$0.3 dex, an amount which is not enough to account for the mean 1 dex offset of $>10^{12}\ L_\odot$ galaxies from the Meurer relation. Further, as we show in Section 6, the relationship between bolometric luminosity and dust attenuation implies that ultraluminous infrared galaxies (ULIRGs) with $L_{\rm bol} \gtrsim 10^{12}\ L_\odot$ on average will have fainter observed UV luminosities, and thus IRX ratios that are boosted, relative to LIRGs. Consequently, the bias of galaxies with $L_{\rm bol} > 10^{12}\ L_\odot$ to have UV slopes that systematically

[13] Note that Meurer et al. (1999) use a different definition of IRX than used here. They define IRX as the ratio of FIR-to-UV flux density, where $L_{\rm IR} \approx 1.75 \times L_{\rm FIR}$ based on the calibration of Calzetti et al. (2000). We have applied this correction to the Meurer relation before comparing to our data.

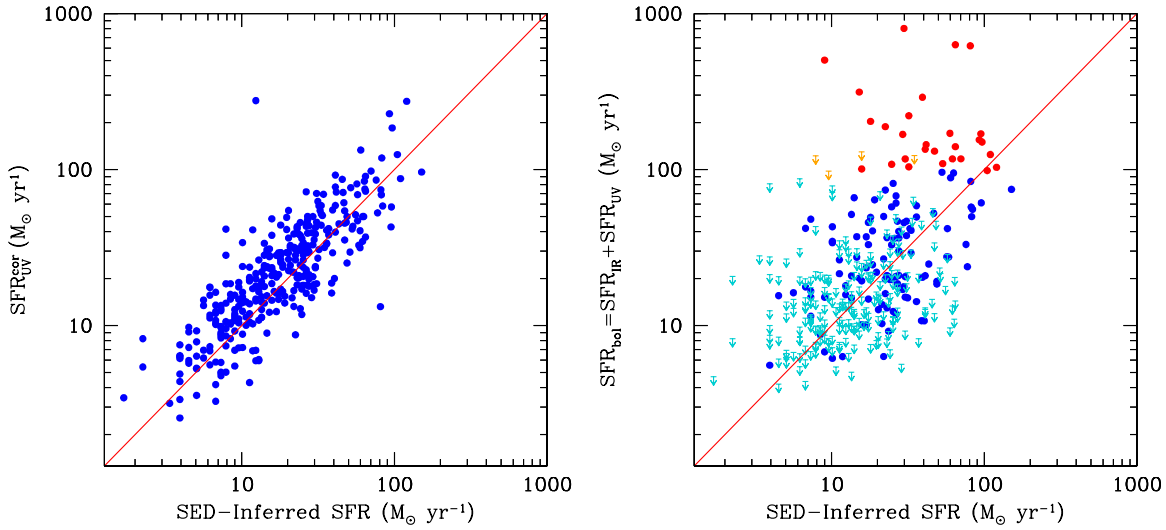

Figure 8. Left: dust-corrected UV estimate of the star formation rate (SFR; assuming the Meurer relation) vs. the SED-derived star formation rates. All SFRs assume a Chabrier IMF. Right: bolometric SFR, defined as the sum of the IR and UV-derived SFRs, vs. the SED-derived SFRs. Orange and red points indicate galaxies with bolometric luminosities $L_{\rm bol} \geqslant 10^{12}\ L_\odot$.

(A color version of this figure is available in the online journal.)

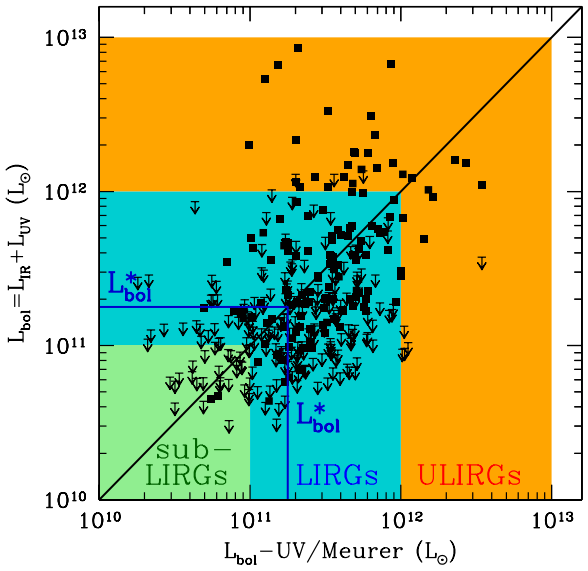

Figure 9. Comparison between the direct tracer of bolometric luminosity ($L_{bol} = L_{IR} + L_{UV}$) and that obtained by combining L_{UV} with the Meurer prediction of the dust attenuation.

(A color version of this figure is available in the online journal.)

underestimate their attenuation is likely to be a physical effect, as opposed to one driven by luminosity-dependent biases in the calibrations between mid-IR and total-IR luminosity.

Deviation of the these ULIRGs from the Meurer relation can be seen more clearly in Figure 9, where we compare the direct tracer of bolometric luminosity (sum of infrared and UV luminosities) with that obtained when we combine the UV luminosity with the Meurer prediction for the dust attenuation. Over the luminosity range probed by the data, the Meurer relation successfully predicts the bolometric luminosity for LIRGs, but significantly underpredicts the luminosity of ULIRGs. This naturally translates to a disagreement between the SED-derived SFRs and those derived from summing the IR and UV-based SFRs for ULIRGs at these redshifts, since the SED-derived SFRs assume the Calzetti extinction curve (right panel of Figure 8). The critical point is that the Meurer relation can be used reliably up to $L_{bol} \simeq 10^{12}\ L_\odot$ at $z \sim 2$, and thus is valid for typical star-forming galaxies at these redshifts.

5.3. Young Galaxies with Inferred Star-formation Ages of $\lesssim$100 Myr

We now turn to the 49 galaxies with ages $\lesssim$100 Myr; this young sample constitutes ≈13% of the sample of 392 galaxies. Only 4 of the 49 galaxies are detected directly at 24 μm (Figure 10). About three-fourths of the young galaxies undetected at 24 μm have limits in IRX that imply that they lie below the Meurer relation. Stacking the 24 μm data results in a conservative 5σ limit in IRX that suggests that these young galaxies are in general less attenuated than their older counterparts at a fixed value of β. This result is further supported by a stack of the X-ray data for the 31 young galaxies in the GOODS-N field that places a 5σ upper limit in IRX that is still 0.5 dex lower than the Meurer expectation.

These observations suggest that an SMC-like (as opposed to a Calzetti) extinction curve may be more appropriate in describing young galaxies in our sample. Because the ages are derived from the stellar population modeling (Section 3) and are therefore degenerate with respect to the assumed extinction curve (Calzetti), it seems prudent to determine how the inferred ages are perturbed under the assumption of an SMC extinction curve. Adopting an SMC curve will generally yield older ages relative to the Calzetti assumption because in the SMC case a smaller fraction of the optical minus near-infrared color is attributed to dust and a larger fraction is attributed to an older stellar population (e.g., Shapley et al. 2001).

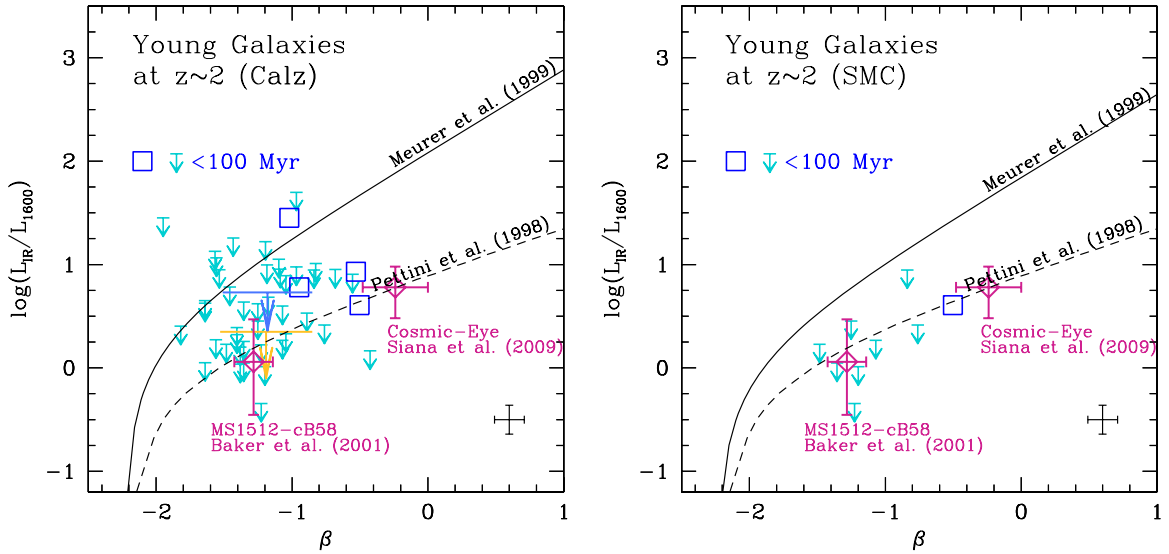

Figure 10. Same as Figure 6 for galaxies younger than 100 Myr, where ages are determined from stellar population modeling assuming the Calzetti (left panel) and SMC (right panel) extinction curves. The open squares and small downward-pointing arrows denote galaxies detected and undetected, respectively, at 24 μm. The large light blue and yellow downward-pointing arrows denote the 5σ limits from stacks of the 24 μm and X-ray data, respectively, for the <100 Myr galaxies. Also shown are direct measurements based on CO and *Spitzer* IRS observations of the two lensed LBGs, MS1512−cB58 and the Cosmic Eye, and the form of the SMC extinction curve presented in Pettini et al. (1998). There are fewer points in the right panel since ages determined with the SMC curve are generally older than those derived with the Calzetti curve. Thus, the fraction of galaxies considered "young" (<100 Myr) is significantly smaller for the SMC case relative to the Calzetti case (see the text).

(A color version of this figure is available in the online journal.)

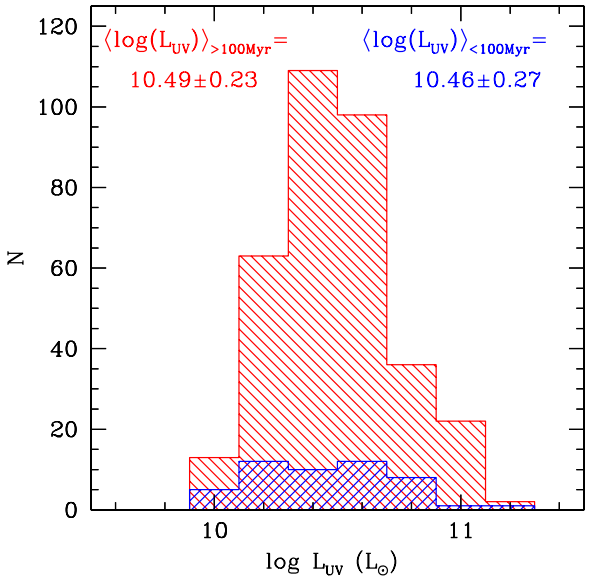

Figure 11. UV luminosity distribution of galaxies with ages less than and older than 100 Myr.

(A color version of this figure is available in the online journal.)

The results obtained by adopting an SMC curve are summarized in Figure 10. As expected, the fraction of galaxies considered "young" ($\lesssim$100 Myr) is a factor of five times lower (9/392) than that obtained with a Calzetti curve. More relevant to our discussion here is that even when considering an SMC curve, we note a significant departure of the youngest galaxies from the locus of points that are characteristic of older galaxies in the IRX–β plane that lie on the Meurer relation. At face value, these arguments may seem a bit circular given the degeneracy between the assumed extinction law and inferred ages. However, both IRX and β are determined *independently* of the stellar population modeling and Figure 10 demonstrates clearly that irrespective of the choice of extinction curve, the IRX–β properties of the youngest galaxies deviate from those of older, more typical ones at $z \sim 2$ (cf., Figure 6).

5.3.1. 24 μm Detection Fraction and β Distribution

The differences between the young and old populations are demonstrated more clearly in Figure 7 where we show the 24 μm detection fraction for the young galaxies versus older more typical star-forming galaxies. While the detection fraction for typical star-forming galaxies increases steadily with β, that same fraction for the young galaxies stays essentially flat (with no detected objects). The only young galaxies detected directly at 24 μm are those with the reddest spectral slopes. Because the redshift and UV luminosity distributions of galaxies in the young and typical subsamples are not substantially different (Figure 11), the trend between detection frequency and UV slope implies that the youngest galaxies are less infrared luminous and less dusty on average than typical galaxies at a fixed β. Note further that the distributions of spectral slopes for the older and younger subsamples are unlikely to have been drawn from the same parent distribution. A K–S test implies a probability $P \simeq 0.005$ that the β distribution of young galaxies is drawn from the same parent distribution as that of the older galaxies. Thus, our analysis implies that the youngest galaxies are not only less infrared luminous and less dusty on average than older galaxies with the same range in β, but they also tend to have redder spectral slopes than older galaxies. The difference in mean β between galaxies with ages $\leqslant$ 100 Myr and $>$100 Myr is $\langle\beta\rangle_{\leqslant 100\,\mathrm{Myr}} - \langle\beta\rangle_{>100\,\mathrm{Myr}} = 0.26$. The apparently contradictory results that the young galaxies have both redder spectral slopes *and* are on average less dusty than typical galaxies may be understood if the reddening curve of the young galaxies is "steeper" (i.e., less dust is required to redden the continuum) in the UV than the typically assumed Meurer/Calzetti relations, as alluded to above. To rule out any biases that may underlie the offset of these galaxies from the Meurer relation, we must scrutinize the validity of the measures of attenuation for such young galaxies, as we discuss next.

5.3.2. Measures of L_{IR} in Young Galaxies

There are several independent reasons to suspect that the $L_{\rm IR}$ we compute for these young galaxies are not biased by the way in which we are measuring them. We consider first the possibility that galaxies with ages $\lesssim$100 Myr have systematically lower $L_8/L_{\rm IR}$ ratios than their older counterparts. Specifically, it is thought that much of the carbon dust in the interstellar medium (ISM) is ejected from AGB stars on timescales of $\simeq$200 Myr, whereas the larger dust grains responsible for the bulk of the IR emission are produced on the much shorter timescale of Type II supernovae (SNe). Local observations appear to support this scenario in the sense that PAH metallicity ($Z_{\rm PAH}$) is observed to be significantly lower relative to the IR dust grain metallicity ($Z_{\rm dust}$) for metal-poor galaxies, but that the ratio of the metallicities increases rapidly until an equilibrium is reached for gas-phase metallicities ($Z_{\rm gas}$) in excess of $\approx$0.3 $Z_\odot$, owing to increased carbon ejection by AGBs (Galliano et al. 2008). This delayed injection of carbon grains results in a depressed ratio of mid-IR to total-IR flux for galaxies younger than 200 Myr. However, direct measurements of the mid-IR spectral features from *Spitzer* IRS spectra and long wavelength ($\gtrsim$70 μm) constraints on the infrared luminosities of two young ($\lesssim$300 Myr) lensed LBGs at $z \sim 3$ (MS1512−cB58 and the "Cosmic Eye") imply $L_8/L_{\rm IR}$ ratios that are similar to those of local star-forming galaxies and high-redshift submillimeter galaxies (Siana et al. 2008, 2009), and older LBGs at $z \sim 2$–3 (Reddy et al. 2006a). In addition, an independent deduction based on CO observations of MS1512−cB58 (Baker et al. 2001) points to an $L_{\rm IR}$ that is not significantly different than what we would have predicted from our calibration between L_8 and $L_{\rm IR}$. Further, if we restrict the local correlation between $Z_{\rm PAH}$, $Z_{\rm dust}$, and $Z_{\rm gas}$ to the same dynamic range in gas-phase metallicity as observed among LBGs at $z \sim 2$, $0.3 \lesssim Z_{\rm gas} \lesssim Z_\odot$ (Erb et al. 2006a), we would find a PAH to dust grain metallicity ratio that is roughly constant. The limited dynamic range in gas-phase metallicity probed by the current sample, as well as the direct measurements of the PAH to IR ratio in lensed LBGs at $z \sim 3$, suggests that our conversion between L_8 and $L_{\rm IR}$ (calibrated primarily on galaxies older than 100 Myr) should be a reasonable approximation for the younger galaxies as well. In this case, the mid-IR emission observed in the young galaxies may be due to some combination of silicate and amorphous carbon dust produced in Type II SNe (Todini & Ferrara 2001; but see Kotak et al. 2009 and references therein).

Finally, the X-ray data provide an independent confirmation of our results. The X-ray emission in starburst galaxies arises primarily from shock-heated outflowing gas (Strickland et al. 2004; Grimes et al. 2005, 2006) and high-mass X-ray binaries (Ghosh & White 2001), both of which should be sensitive to star formation on relatively short timescales ($\simeq$70 Myr) that are comparable to the dynamical timescale noted above.

Consequently, if the true infrared luminosities of the young galaxies were larger than what we infer from L_8 (and if L_{IR} was consistent with the Meurer prediction), then the X-ray stack of the 49 young galaxies should have yielded a significant detection. Yet, we are able to place a firm 5σ upper limit on the X-ray-inferred IRX of $\log(L_{IR}/L_{UV}) < 0.35$.

In summary, galaxies with ages $\lesssim$100 Myr appear to have lower attenuation on average than their UV slopes would imply from the Meurer relation (note that the Meurer and Calzetti relations track each other closely for $\beta > -2.0$). This inference is based on the limited dynamic range in metallicity probed by UV-bright ($\mathcal{R} \lesssim 25.5$) LBGs, direct measurements of L_8 and L_{IR} in at least a couple of young lensed LBGs, stacked X-ray measurements, and the 24 μm detection fraction as a function of UV slope. Similar conclusions are reached by R06 and Siana et al. (2008, 2009). We have shown here that this result appears to apply generically to most young $\lesssim$100 Myr galaxies at $z \sim 2$. The small fraction of young galaxies that have red β and are detected at 24 μm points to a scatter in IRX for young galaxies that may be larger than for their older counterparts.[14] Direct detection of the dust emission of a statistical sample of young high-redshift galaxies is required to accurately constrain their scatter in attenuation.

We conclude by noting the following. First, only 10 of the 90 galaxies used to constrain the relation between L_8 and $L(\mathrm{H}\alpha)$ have (Calzetti-derived) ages <100 Myr, and redetermining the relation excluding these 10 sources does little to affect the overall fit between L_8 and $L(\mathrm{H}\alpha)$. In other words, our assumption of the Calzetti relation in dust correcting the Hα luminosities for these sources minimally affects our conversion between L_8 and L_{IR}. Second, when computing bolometric SFRs, the overestimation of attenuation by applying the Meurer/Calzetti relations may be partly compensated for by the fact that the UV luminosities in young galaxies will *underpredict* the SFR. The latter effect is due to the fact that for a CSF history the ratio of O and B stars contributing to the UV continuum will stabilize only after the main-sequence lifetime of B stars of $\simeq$100 Myr. This underscores the need to correct for both a different attenuation and a different conversion between UV luminosity and SFR when inferring the total SFRs of young galaxies (ages $\lesssim$100 Myr) at high redshift.

5.4. Summary

We have used the relationship between L_8, SFR, and L_{IR} to examine the variation of UV slope with dust attenuation for typical galaxies, bolometrically luminous ones, and the youngest galaxies at $z \sim 2$. We find a significant correlation between UV slope and attenuation for the vast majority of typical star-forming galaxies at $z \sim 2$. In this case, the UV slope can be used to recover dust attenuation to within a scatter of 0.4 dex. Those galaxies with bolometric luminosities in excess of 10^{12} $L_\odot$ have dust obscurations that exceed by almost a decade those predicted from the UV slope, owing to the larger fraction of obscured luminosity in these galaxies and, as we show in Section 6, a decrease in observed UV luminosity relative to galaxies with moderate bolometric luminosities.

Finally, for the $\lesssim$13% of our sample (exact fraction depends on the extinction law used to model the galaxies' photometry; see discussion above) that consists of young galaxies with ages $\lesssim$100 Myr, the local correlation overpredicts dust attenuations at a given β. This implies that such young galaxies may on average follow an extinction curve that deviates from the usually assumed Meurer/Calzetti. These results are similar to what we found previously based on a smaller sample of galaxies in the GOODS-North field (R06). Here, we have expanded these initial results by exploring in more detail some of the systematics that may give rise to such an offset. We find that the undetected young galaxies and the two lensed LBGs from the literature exhibit β and IRX that are consistent with an SMC dust extinction curve (e.g., Pettini et al. 1998). This behavior may be due to a difference in covering fraction of dust, where the younger galaxies have larger covering fractions consistent with a foreground screen of dust as described by an SMC-like extinction curve. Alternatively, we cannot rule out the possibility that the dissimilar extinction curve for young galaxies may arise from differences in the dust grain size distribution. This may be the case if the dust giving rise to the mid-IR emission in young galaxies is produced primarily in Type II SNe and contrasts in size and composition from dust produced in lower mass stars (e.g., Maiolino et al. 2004; Todini & Ferrara 2001; see also discussion in Siana et al. 2009).

6. RELATIONSHIP BETWEEN BOLOMETRIC LUMINOSITY AND DUST ATTENUATION

Employing our measures of the dust obscuration and bolometric luminosities for typical star-forming galaxies at $z \sim 2$, we proceed to examine the relationship between these two quantities, its implication for the correlation between UV and bolometric luminosity, and its redshift evolution.

6.1. Functional Form and β Dependence

Based on the sample of 392 galaxies with MIPS observations, we find a strong correlation between L_{bol} and dust attenuation with a formal scatter of 0.23 dex about a linear fit (Figure 12). The fit to the present data is essentially identical to the linear fit to a smaller sample in the GOODS-N field (R06), despite the differences in the conversion between L_8 and L_{IR} used in the current versus previous (R06) study. This similarity (and the small scatter) is due to the fact that $L_{bol} = L_{IR} + L_{UV}$ is highly correlated with dust attenuation, L_{IR}/L_{UV}, according to our definitions. Nonetheless, we are confident of our calibration between bolometric luminosity and dust attenuation given that L_{bol} estimated from the sum of the IR and UV luminosities is consistent with L_{bol} (or SFR) estimated from X-ray data and from the dust-corrected Hα and UV luminosities (Section 4.2). Further, R06 showed that the relationship between L_{bol} and L_{IR}/L_{UV} for UV-selected samples remains valid for star-forming galaxies selected on their rest-frame optical colors and/or submillimeter emission. More recently, Huang et al. (2009) find that IRAC-selected ULIRGs at $z \sim 1.9$ lie on the same relation as defined by the typically less luminous UV-selected galaxies (LIRGs). These results imply that for the observationally accessible area of the L_{bol}–L_{IR}/L_{UV} plane, the relationship defined by UV-selected galaxies is not substantially different or biased with respect to that defined by galaxies selected by other means (e.g., optical and IR selections). Formally, our best-fit relation between L_{bol} and dust obscuration is

$$\log[L_{bol}/L_\odot] = (0.69 \pm 0.03)\log[L_{IR}/L_{UV}] + (10.91 \pm 0.04) \quad \text{for } L_{UV} \gtrsim 10^{10}\ L_\odot. \tag{4}$$

Similar relations between bolometric luminosity, or SFR, and dust attenuation have been found at low and high redshifts (Wang

[14] For example, applying the Meurer relation to one young LBG at $z = 2.83$ ("Westphal-MM8") results in a bolometric luminosity similar to that inferred from its detection at 850 μm (Chapman & Casey 2009).

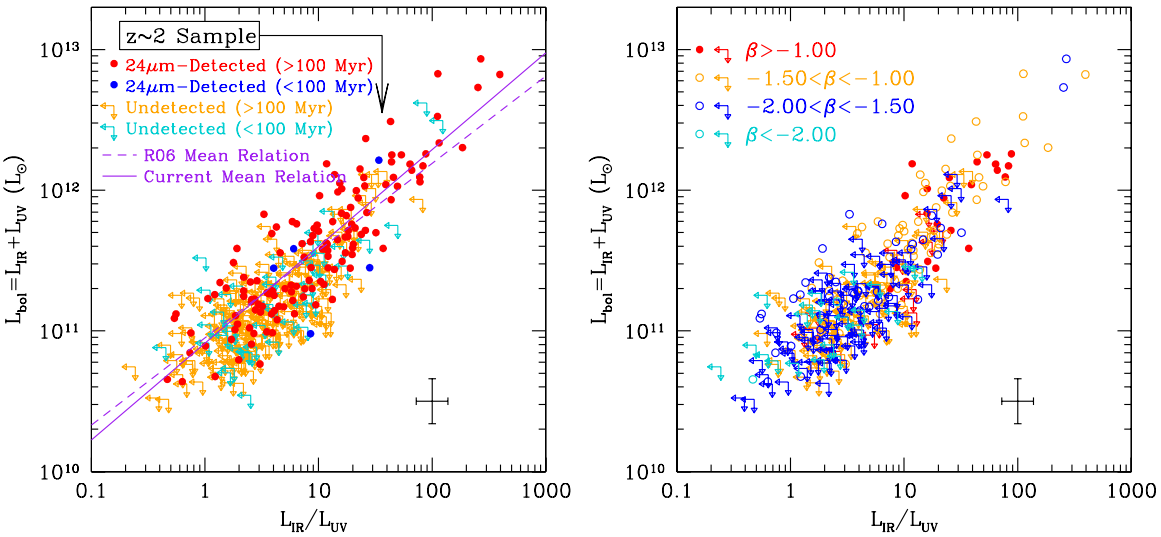

Figure 12. Left: bolometric luminosity vs. dust attenuation for the sample of 392 galaxies with spectroscopic redshifts between $1.5 < z < 2.6$. Right: same as left panel but color coded by UV slope β and restricted to galaxies with ages >100 Myr.

(A color version of this figure is available in the online journal.)

& Heckman 1996; Adelberger & Steidel 2000; Reddy et al. 2006b; Buat et al. 2007, 2009; Burgarella et al. 2008).

The variation of spectral slope with attenuation and $L_{\rm bol}$ can be seen in the right panel of Figure 12 where points are color coded by β. Galaxies with red $\beta > -1.00$ are on average more attenuated and more bolometrically luminous than galaxies with bluer β. Galaxies with $-1.50 < \beta \leqslant -1.00$ span a relatively larger range of attenuation and $L_{\rm bol}$, reflecting the fact that many bolometrically luminous galaxies have a similar range in β (but much larger attenuation) than less luminous galaxies (Section 5.2). Galaxies with the bluest β span a narrower range in attenuation and $L_{\rm bol}$, both being on average lower for these galaxies.

6.2. Variation of Observed UV Luminosity with Bolometric Luminosity

6.2.1. Bolometric Luminosities of UV-faint Galaxies

For further insight, we have recast the correlation between bolometric luminosity and dust attenuation (Equation (4)) in terms of the observed UV luminosity ($L_{\rm UV}$),

$$\log[L_{\rm UV}/L_\odot] = \log[L_{\rm bol}/L_\odot] - \log\left[10^{(\log[L_{\rm bol}/L_\odot]-b)/a} + 1\right], \quad (5)$$

where $a = 0.69 \pm 0.03$ and $b = 10.91 \pm 0.04$, as shown in Figure 13. The relationship between $L_{\rm bol}$ and $L_{\rm UV}$ implies that galaxies with faint UV luminosities are less attenuated than their UV-bright counterparts. A recent study based on deep GOODS and UDF ACS finds that UV-faint galaxies at $z \sim 2.5$ have systematically bluer UV slopes (β) relative to UV-bright ones, implying that the former may be less dusty (Bouwens et al. 2009). Further, Reddy et al. (2008) and Reddy & Steidel (2009) argue based on physical reasons that such UV-faint galaxies are unlikely to be as attenuated on average as their UV-bright counterparts. For example, significant amounts of dust in these galaxies, combined with their large number densities as inferred from the steep faint-end slope of the UV LF, would result in stellar mass densities and an infrared background significantly in excess of those measured (Reddy &

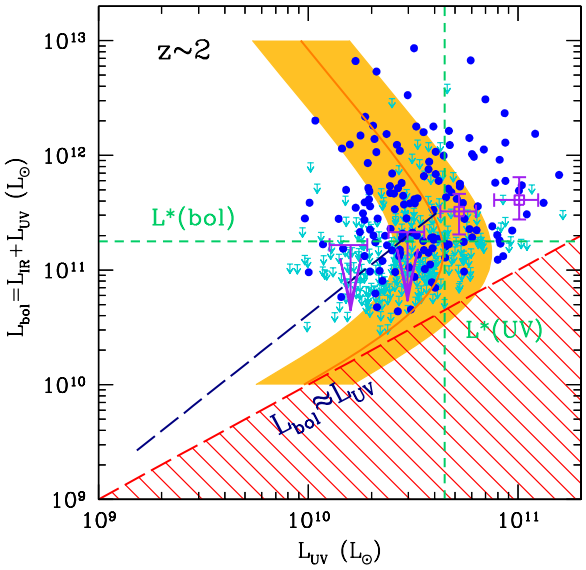

Figure 13. Bolometric luminosity ($L_{\rm bol}$) vs. observed UV luminosity ($L_{\rm UV}$). Small points and arrows indicate galaxies detected and undetected, respectively, at 24 μm. The 24 μm stacked results are shown by the open squares and large arrows (purple). The shaded region denotes $\pm 1\sigma$ about the mean relation implied by the correlation between $L_{\rm bol}$ and dust attenuation (Equation (4)). The hashed region indicates the area excluded by the fact that $L_{\rm bol}$ must be greater than $L_{\rm UV}$. The dashed horizontal and vertical lines delineate the values of $L^*_{\rm UV}$ and $L^*_{\rm bol}$ at $z \sim 2$ (Reddy & Steidel 2009; Reddy et al. 2008), and the thick dashed line shows the extrapolation of the relation to UV-faint galaxies (see the text).

(A color version of this figure is available in the online journal.)

Steidel 2009). Taking this luminosity-dependent dust correction into account, Reddy et al. (2008) and Reddy & Steidel (2009) demonstrate that such UV-faint galaxies dominate the bolometric luminosity density at $z \sim 2$–3.

Our present (larger) data set suggests a significant dependence between bolometric and UV luminosity, as evidenced by the trend between 24 μm nondetection fraction and UV luminosity (Figure 14). Specifically, this trend implies that galaxies with faint $L_{\rm UV}$ are also on average less IR luminous, in turn suggesting that they are less bolometrically luminous, than their UV-bright

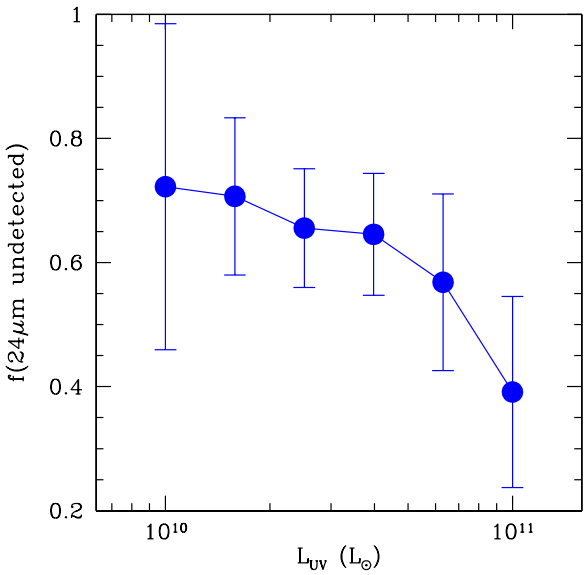

Figure 14. 24 μm nondetected fraction as a function of unobscured UV luminosity ($L_{\rm UV}$). Error bars assume Poisson statistics.

(A color version of this figure is available in the online journal.)

counterparts. The trend between 24 μm nondetection fraction and $L_{\rm UV}$ is further supported by a stacking analysis. Specifically, we stacked the 24 μm data in bins of $L_{\rm UV}$, including both detections and nondetections, and limited the stack to galaxies with $L_{\rm bol} < 10^{12}\ L_{\odot}$. The latter restriction is imposed because we are interested in determining whether a trend exists between dustiness and UV luminosity for *typical* galaxies at $z \sim 2$ (i.e., excluding bolometrically luminous galaxies with values of $L_{\rm UV}$ similar to those of galaxies with lower $L_{\rm bol}$). These stacked results yield average $L_{\rm bol}$ consistent with the prediction from combining the Meurer relation with the trend between UV slope and continuum magnitude (e.g., Bouwens et al. 2009), as illustrated in Figure 13. Thus, our present sample provides the first direct evidence (independent of the UV slope) for a trend between UV luminosity on the one hand, and bolometric luminosity and dust obscuration on the other.

At first glance, these results run counter to our previous analysis that indicated no correlation between dustiness and UV magnitude for UV-bright ($\mathcal{R} < 25.5$) galaxies (Reddy et al. 2008). More specifically, in the previous analysis of the GOODS-North field, the stacked values of $L_{\rm IR}/L_{\rm UV}$ as a function of UV magnitude had uncertainties that were sufficiently large that we could not rule out the possibility of no trend between dustiness and UV magnitude (see Figure 11 of Reddy et al. 2008; see also discussion in Section 6.5). Note that despite this lack of trend observed with the smaller sample, we investigated in detail the systematics introduced by assuming various relations between dustiness and UV luminosity extending from UV-bright galaxies (for which empirical constraints on the dust obscuration factors exist) to UV-faint galaxies (see Reddy et al. 2008; Reddy & Steidel 2009). The variation of IR and bolometric luminosity with UV luminosity becomes more apparent with our larger sample (Figures 13 and 14, Section 6.5).

6.2.2. Saturation of UV Luminosity

The shallower-than-unity slope of the relationship between $L_{\rm bol}$ and dust obscuration implies that the UV luminosity turns over or "saturates," at which point any additional star formation will be optically thick (Figure 13). As we discuss below, this saturation of the UV luminosity with increasing SFR likely explains why no correlation was found previously between $L_{\rm bol}$ and $L_{\rm UV}$ (e.g., as can also be seen by the scatter of the points in Figure 13) since these spectroscopic samples probe a relatively narrow range of UV luminosity around the value of $L^*_{\rm UV}$. The saturation point can only be ascertained from the functional fit to the $L_{\rm bol}$–$L_{\rm IR}/L_{\rm UV}$ relation and should become more apparent with future measurements of the dust attenuation of galaxies fainter than our spectroscopic limit. In any case, galaxies routinely found in *Spitzer* surveys at high redshift (e.g., ULIRGs) are typically fainter in the UV than moderately luminous galaxies found in optical surveys (e.g., LIRGs). As noted above, such ULIRGs appear to follow the same $L_{\rm bol}$–dustiness relation as UV-selected galaxies. These results can be understood if the dust obscuration, $L_{\rm IR}/L_{\rm UV}$, increases more rapidly than the increase of *total* UV luminosity as the bolometric luminosity increases. This may largely explain why ULIRGs have IRX ratios far in excess of the values predicted by their UV spectral slopes based on the Meurer relation (Section 5, Figure 9). The turnover in $L_{\rm UV}$ implies that even in the presence of galaxies with very large SFRs at $z \sim 2$, the observed UV luminosity will never be brighter than a certain value which, at $z \sim 2$, corresponds to $L_{\rm UV} \approx 10^{11}\ L_{\odot}$.

6.2.3. Implications for the Shape of the UV LF

The connection between UV and bolometric luminosity has important implications for the shape of the UV luminosity function. In particular, the saturation point for the observed UV luminosity occurs approximately at the values of $L^*_{\rm UV}$ and $L^*_{\rm bol}$ at $z \sim 2$. This is not surprising because, by definition, L^* is the point brighter than which the number density of sources decreases exponentially. This effect can also be seen by comparing our previous determinations of the UV LF, which is well described by a Schechter function, with the bolometric LF, which has a more power-law-like shape and not as well defined of a "knee" (Reddy et al. 2008; Reddy & Steidel 2009). The important point is that the saturation effect is a direct result of the increasing extinction with $L_{\rm bol}$. Consequently, dust obscuration must be the dominant effect in modulating the bright end of the UV LF, and thus dictating the value of L^*, at $z \sim 2$.

6.3. Redshift Evolution

Comparison with the relation derived locally (e.g., Buat et al. 2007) shows that L^* galaxies at $z \sim 2$ exhibit $L_{\rm IR}/L_{\rm UV}$ ratios that are a factor of five times lower than those of local galaxies with a similar $L_{\rm bol}$ (Reddy et al. 2006b, 2008), implying a redshift evolution in the extinction per unit SFR (or per unit $L_{\rm bol}$). R06 suggested that this may reflect either an evolution in the dust-to-gas ratios as galaxies age or a change in the average sizes of the infrared and UV emitting regions of galaxies with redshift. In the following, we discuss the importance of the $L_{\rm UV}$ limit in accurately assessing this evolution, a consideration of the $L_{\rm bol}$–$L_{\rm IR}/L_{\rm UV}$ relation for UV-faint galaxies at high redshift, and the implications of these results for the evolution of individual galaxies.

6.3.1. Dependence on L_{UV} Limit

Quantifying properly the evolution in the $L_{\rm bol}$–$L_{\rm IR}/L_{\rm UV}$ relation requires a careful consideration of the $L_{\rm UV}$ limit used to compare samples at different redshifts (see also the discussion in Buat et al. 2009). The strong redshift evolution in $L^*_{\rm UV}$ (Reddy & Steidel 2009) implies that a relatively shallow UV luminosity

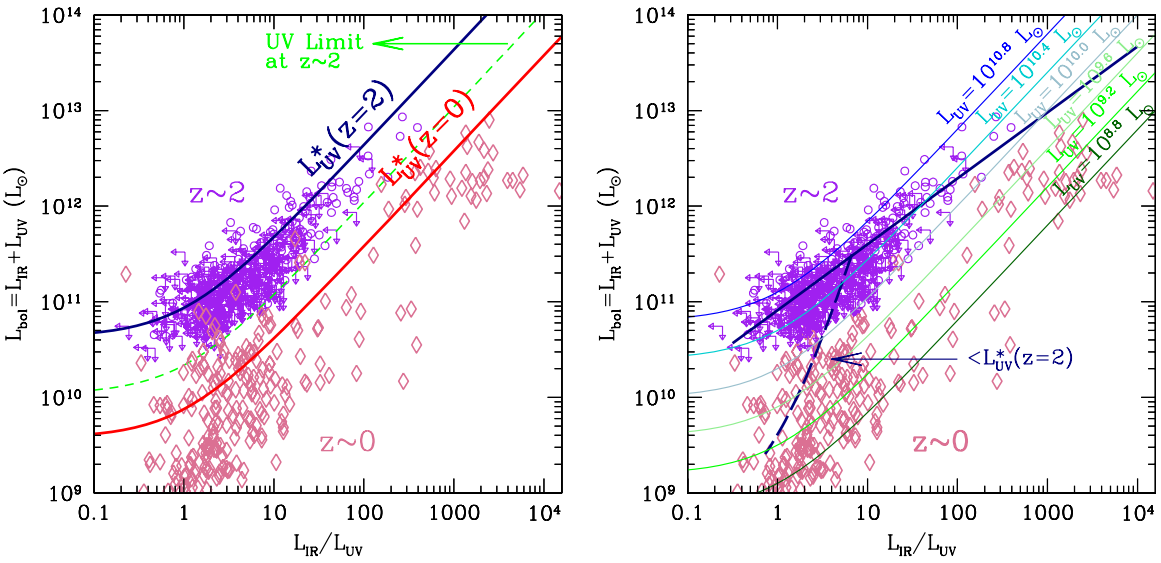

Figure 15. Left: bolometric luminosity vs. dust attenuation for our $z \sim 2$ sample compared with that of local galaxies from Bell (2003), Brandl et al. (2006), and Huang et al. (2009). Also shown are lines of constant UV luminosity at the value of $L^*_{\rm UV}$ at $z = 2$ and $z = 0$ (solid lines), and the UV spectroscopic limit at $z \sim 2$ (dashed line). Right: same as left panel, in addition to the best-fit relation between bolometric luminosity and dust attenuation for $L_{\rm UV} \gtrsim 10^{10}$ $L_\odot$ at $z \sim 2$ (thick solid line) and its extension to UV-faint galaxies (thick dashed line). Also shown are lines of constant UV luminosity for $L_{\rm UV} = 10^{8.8}$–$10^{10.8}$ $L_\odot$.
(A color version of this figure is available in the online journal.)

limit will exclude the parameter space in the $L_{\rm bol}$–$L_{\rm IR}/L_{\rm UV}$ plane where most normal galaxies in the local universe lie (Figure 15), causing one to infer a milder redshift evolution in the extinction per unit SFR. It is clear that an accurate comparison of these relations for typical galaxies requires a $L_{\rm UV}$ limit that is sufficiently faint to detect these average ($L^*_{\rm UV}$) galaxies at all redshifts in question. A sufficiently faint $L_{\rm UV}$ limit reveals that $L^*_{\rm UV}$ galaxies at $z \sim 2$ are a factor of $\approx$10 times less attenuated than local galaxies of the same $L_{\rm bol}$ (Figure 15).

6.3.2. Consideration of UV-faint Galaxies at High Redshift

Clearly, the $L_{\rm UV}$ limit is also an important consideration in our interpretation of the $L_{\rm bol}$–$L_{\rm IR}/L_{\rm UV}$ relation at $z \sim 2$. This limit is defined by the magnitude cut of our spectroscopic sample ($\mathcal{R} = 25.5$) and corresponds to $L_{\rm UV} \approx 10^{10}$ $L_\odot$ (Figures 11 and 15). This limit is faint enough to detect $L^*_{\rm UV}$ galaxies at $z \sim 2$, where $L^*_{\rm UV}$ is determined not from the present sample alone, but from a consideration of the UV luminosity function measured using data extending 1.5 mag fainter than our spectroscopic limit (Reddy & Steidel 2009). Therefore, the $L_{\rm bol}$–$L_{\rm IR}/L_{\rm UV}$ relation derived here is not just valid for the sample analyzed here, but valid for $L^*_{\rm UV}(z = 2)$ galaxies in general. The saturation of $L_{\rm UV}$ discussed above can also be seen in Figures 15 and 16 where the relation between $L_{\rm bol}$ and $L_{\rm IR}/L_{\rm UV}$ at $z \sim 2$ crosses the same line of constant $L_{\rm UV}$ more than once.

Let us now consider how the $L_{\rm bol}$–$L_{\rm IR}/L_{\rm UV}$ relation may change for galaxies fainter than the $L_{\rm UV} \approx 10^{10}$ $L_\odot$ threshold. Our finding of lower bolometric luminosities for UV-faint galaxies (Section 6.2) suggests that extending the $L_{\rm UV} \approx 10^{10}$ $L_\odot$ limit to fainter luminosities is unlikely to reveal a very large population of UV-faint galaxies with $L_{\rm bol}$ similar to those of UV-bright ones. Therefore, the $L_{\rm bol}$–$L_{\rm IR}/L_{\rm UV}$ relation is unlikely to be significantly broader at $L_{\rm bol} \sim 10^{11}$–10^{12} $L_\odot$ than what we have measured from the spectroscopic sample.

We have illustrated this point by using the relation between UV luminosity and β (Bouwens et al. 2009) to infer the dust attenuation and bolometric luminosities using the Meurer

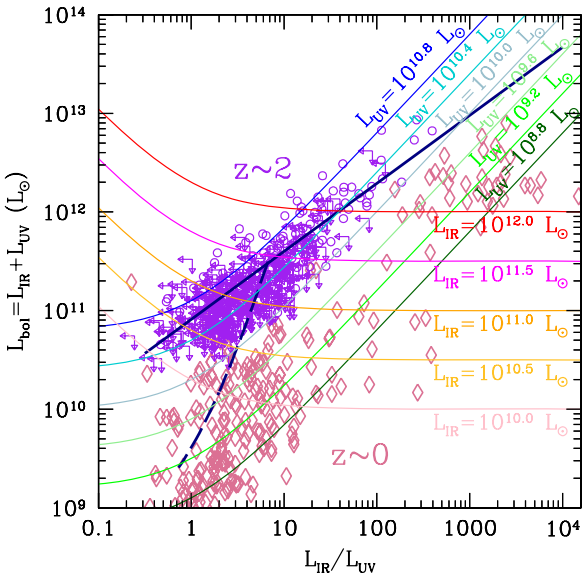

Figure 16. Same as Figure 15 showing lines of constant $L_{\rm UV}$ and $L_{\rm IR}$ luminosity.
(A color version of this figure is available in the online journal.)

relation, thus extending our measurement of the $L_{\rm bol}$–$L_{\rm IR}/L_{\rm UV}$ relation to UV-faint galaxies (Figure 15). Examined over a wider range in UV luminosity, it becomes clear that the $L_{\rm bol}$–$L_{\rm IR}/L_{\rm UV}$ relation at $z \sim 2$ is defined by a sequence of galaxies with increasing $L_{\rm bol}$ and $L_{\rm IR}/L_{\rm UV}$ with increasing UV luminosity.

6.3.3. Evolution of Individual Galaxies

Figure 16 highlights another important issue. While the dustiness of galaxies of a given $L_{\rm bol}$ increases with decreasing redshift, this should not be misconstrued to suggest that a typical $z \sim 2$ galaxy will evolve to become dustier but retain the same $L_{\rm bol}$. Clustering analyses of L^* galaxies at $z \sim 2$ imply that they evolve to reside in the bulges of spirals and low-mass ellipticals by $z \sim 0$ (Conroy et al. 2008). Therefore, the evolutionary track

of any *single* galaxy in the $L_{\rm bol}$–$L_{\rm IR}/L_{\rm UV}$ plane is unlikely to be perpendicular to either axis. As galaxies on average fade between $z \sim 2$ and the present day, reflecting the global decline of the SFR density (e.g., Reddy & Steidel 2009; Reddy et al. 2008; Madau et al. 1996; Giavalisco et al. 1996; Steidel et al. 1999), there will be a corresponding decrease in their $L_{\rm UV}$ and $L_{\rm IR}$, and hence $L_{\rm bol}$. The critical point is that without taking into account the offset between the $z \sim 2$ and $z \sim 0$ relations, one would wrongly conclude that the dustiness observed in local $L^*_{\rm bol}$ galaxies is similar to that observed for galaxies of the same bolometric luminosity at $z \sim 2$, when in fact the dustiness is lower at a fixed $L_{\rm bol}$ at higher redshift.

The correlation between bolometric luminosity and dust attenuation simply reflects the relationship between SFR and gas surface density, i.e., the Schmidt law (Zoran et al. 2006). An increase in the dust-to-gas ratio with galaxy age would simply shift this relationship with redshift, as is observed (Reddy et al. 2006b; Buat et al. 2007; Zoran et al. 2006). In Section 7, we revisit the variation of bolometric luminosity with dust attenuation in the context of the oxygen abundances of starburst galaxies. Geometrical effects are also likely to play an important role in the offset between the $z \sim 2$ and $z \sim 0$ relations. For instance, in Figure 16, many of the $z \sim 0$ galaxies with $L_{\rm bol} \sim 10^{10}\ L_\odot$ are bulge-dominated spirals with star formation extending on scales of several tens of kpc. If most of the star formation occurs in the more metal-poor parts of the galactic disks (Pilyugin et al. 2004; Zaritsky et al. 1994; Vila-Costas & Edmunds 1992), then the measured $L_{\rm IR}/L_{\rm UV}$ ratios would be significantly lower than what we would infer based on the globally averaged dust-to-gas ratio, including the metal-rich component associated with the bulge.

6.3.4. Comparison with the Local IUE Sample

The conclusion from the above observations is that some combination of dust-to-gas ratio and size evolution will drive the observed progression of the $L_{\rm bol}$–$L_{\rm IR}/L_{\rm UV}$ relation with redshift. A consequence of this evolution is that we expect to see an offset in the metallicity–luminosity relation with redshift, which we discuss in Section 7. In practice, this redshift evolution in the extinction per unit SFR implies that rest-UV selection allows one to access galaxies with an increasingly larger range in $L_{\rm bol}$ with increasing redshift. The increasing UV transparency with redshift was noted by Adelberger & Steidel (2000) and Reddy et al. (2006b) for UV-selected samples and shown to be true for galaxies selected using other rest-optical and submillimeter flux criteria as discussed in Reddy et al. (2006b). Daddi et al. (2007) also discuss this issue in the context of the differences between local and high-redshift ULIRGs. The increasing dynamic range in bolometric luminosity probed by UV selection is demonstrated more directly in Figure 17 where we compare typical galaxies at $z \sim 2$, for which the Meurer relation is found to be valid, with many of the same galaxies that were used to calibrate the Meurer et al. (1999) relation locally; the latter sample is drawn from observations with the *International Ultraviolet Explorer* (*IUE*; Kinney et al. 1993; Heckman et al. 1998; Meurer et al. 1999). Galaxies that were used to calibrate the Meurer relation locally span the same range of IRX ($L_{\rm IR}/L_{\rm UV}$) as L^* galaxies at $z \sim 2$, yet the local sample spans luminosities that are anywhere from one to two decades less luminous at a fixed $L_{\rm IR}/L_{\rm UV}$. The Meurer relation appears to hold for typical galaxies at $z \sim 2$ despite the fact that the relation was calibrated on local galaxies that were significantly less luminous. This suggests that the UV SED alone

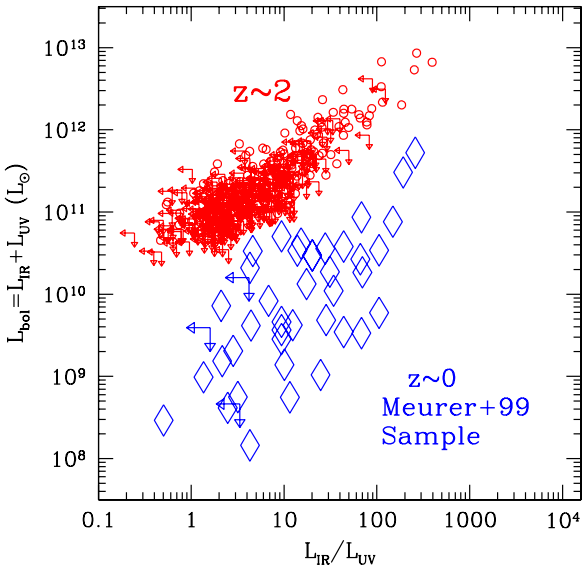

Figure 17. Bolometric luminosity vs. dust obscuration of the $z \sim 2$ sample, compared to that of the local *IUE* sample that was used in large part to calibrate the Meurer et al. (1999) relation.

(A color version of this figure is available in the online journal.)

can be used to recover the total dust attenuation in galaxies with progressively larger $L_{\rm bol}$ at higher redshift, given that, at higher redshift, galaxies are more transparent in the UV at a fixed $L_{\rm bol}$ (Figures 9 and 17).

6.4. Variations in L_{IR} and L_{UV} at a Given L_{bol}

The contours of fixed $L_{\rm UV}$ and $L_{\rm IR}$ shown in Figure 16 emphasize the relative change in these quantities as the dustiness is varied at a fixed $L_{\rm bol}$ at $z \sim 2$. At $L_{\rm bol} \gtrsim 2 \times 10^{11}\ L_\odot$, stochastic changes in the dust obscuration (e.g., such as might be expected if the extinction is patchy) result in $L_{\rm UV}$ to vary much more than $L_{\rm IR}$, simply because a larger fraction of the total luminosity is obscured (e.g., see also Adelberger & Steidel 2000). For faint galaxies with $L_{\rm bol} \lesssim 10^{10}\ L_\odot$, an adjustment in the dust attenuation will do little to alter the UV luminosity while $L_{\rm IR}$ changes more dramatically. Of course, none of these observations are particularly surprising, given that as we adjust $L_{\rm UV}$ there must be a corresponding change in $L_{\rm IR}$ to keep $L_{\rm bol}$ constant.

6.5. Comparison with Previous Results

Several times throughout the discussion above we have mentioned the correlation between UV luminosity on the one hand, and bolometric luminosity and dust attenuation on the other. At face value, these results contrast with previous investigations that have found no correlation between UV luminosity and dustiness (Reddy et al. 2006b; Adelberger & Steidel 2000), as discussed briefly in Section 6.2.1. Of course, a constant average dust correction with UV luminosity naturally leads to lower bolometric luminosities with decreasing UV luminosity. It is clear, however, that if UV-faint galaxies are significantly bluer than their brighter counterparts (Bouwens et al. 2009; Reddy et al. 2008; Reddy & Steidel 2009), and their bolometric luminosities are consistent with the Meurer prediction (stacked points in Figure 13), then their average dust obscuration must also be lower (dashed line in Figure 15). Hence, their bolometric luminosities will be correspondingly lower. We find direct evidence of this from the trend between

24 μm detection fraction and UV luminosity (Figure 14), even for the present sample which is larger but covers the same dynamic range in $L_{\rm UV}$ as previous studies (Reddy et al. 2006b; Adelberger & Steidel 2000). The trend between UV luminosity and UV slope was found over a slightly larger dynamic range in $L_{\rm UV}$ than is usually represented in spectroscopic samples (Bouwens et al. 2009).

The limited dynamic range and/or smaller samples may have contributed to the apparent lack of correlation between UV luminosity and dustiness observed before. There are a couple of other reasons why such a correlation may have been difficult to discern in previous studies. The first is that the saturation of $L_{\rm UV}$ occurs at a value that lies in the range of $L_{\rm UV}$ that is typically probed in spectroscopic surveys. In other words, the non-monotonic behavior of $L_{\rm UV}$ with bolometric luminosity for $L_{\rm UV} \gtrsim 10^{11}\ L_{\odot}$, folded in with measurement errors, washes out the underlying trend between $L_{\rm UV}$ and $L_{\rm bol}$. The trend between dustiness and UV luminosity becomes more apparent once galaxies above the saturation point are removed from the analysis (Section 6.2.1). Second, as seen in the previous section, the lack of correlation may be due to the strong variance of $L_{\rm UV}$ with stochastic changes in the dust obscuration for galaxies of moderate (or higher) luminosities (e.g., Adelberger & Steidel 2000). It is clear that with larger samples, superior (direct) tracers of dust emission, and a larger dynamic range, one can obtain a more complete picture of how dust obscuration varies with other galaxy properties.

6.6. Summary

In this section, we have considered the functional form of the correlation between bolometric luminosity and dust obscuration, its consequence for the shape of the UV luminosity function at $z \sim 2$, and its redshift evolution. For galaxies brighter than our spectroscopic limit of $L_{\rm UV} \approx 10^{10}\ L_{\odot}$, we find a tight positive correlation between bolometric luminosity and dust obscuration ($L_{\rm bol}$–$L_{\rm IR}/L_{\rm UV}$). Our sample provides the first direct evidence for the decrease of infrared luminosity with decreasing UV luminosity. Our results suggest that dust obscuration is likely the dominant effect in modulating the bright end of the UV LF as evidenced by the saturation of UV luminosity with increasing SFR. We demonstrate the importance of the $L_{\rm UV}$ limit in quantifying the redshift evolution of the $L_{\rm bol}$–$L_{\rm IR}/L_{\rm UV}$ relation. Using a sufficiently faint limit, we find that L^* galaxies at $z \sim 2$ have dust obscuration ratios ($L_{\rm IR}/L_{\rm UV}$) that are roughly a factor of 10 times lower than those of local galaxies of the same bolometric luminosity. We examine this offset in the context of metallicity in the next section.

7. RELATIONSHIP BETWEEN DUST ATTENUATION AND METALLICITY AT $z \sim 2$

It is clear from the discussion above that an increase in the dust-to-gas ratio with age plays an important role in the observed evolution of the correlation between bolometric luminosity and dust attenuation. More generally, because most of the metals in the ISM will be contained in (or depleted onto) the same dust grains that attenuate starlight, we expect that the dust attenuation should correlate directly with metallicity and hence stellar mass. The near-IR spectroscopic data for LBGs at $z \sim 2$ have been used to constrain their gas-phase metallicities using the [N II]/Hα ratio. Erb et al. (2006a) compute the stellar mass–metallicity relation at $z \sim 2$ in this manner and find that the relation is offset from the local one (Tremonti et al. 2004) such that at a fixed stellar mass galaxies at $z \sim 2$ are $\approx$2 times less metal rich than present-day galaxies. This offset likely reflects the larger gas fractions at a given stellar mass with increasing redshift (see discussion in Erb et al. 2006a).

7.1. Correlation at $z \sim 2$

To test our expectation of a correlation between metallicity and dust attenuation, we have investigated the variation of $L_{\rm IR}/L_{\rm UV}$ with stellar mass for the sample of 392 galaxies (Figure 18). Assuming that the 24 μm-undetected galaxies have a similar scatter in $L_{\rm IR}/L_{\rm UV}$ at a given mass as the 24 μm detected galaxies, we find a scatter between attenuation and stellar mass of $\approx$0.46 dex about a linear fit between the two. The trend between attenuation and mass can be visualized more easily by examining the mean attenuation in bins of stellar mass as inferred from a stacking analysis. To compute the average $L_{\rm IR}/L_{\rm UV}$, we first stacked the 24 μm emission for galaxies in each bin of stellar mass to find their average $L_{\rm IR}$ luminosity. The average $L_{\rm IR}$ luminosity is then combined with the average $L_{\rm UV}$ luminosity for galaxies in each bin of stellar mass to compute the $L_{\rm IR}/L_{\rm UV}$ ratio. The error in the ratio takes into account the error in the stacked estimate of the $L_{\rm IR}$ luminosity and the error in the mean of the $L_{\rm UV}$ luminosity. Doing this, we find that galaxies with stellar masses $\gtrsim 10^{11}\ M_{\odot}$ are roughly 100 times more attenuated on average than those with stellar masses $\lesssim 10^{9.5}\ M_{\odot}$ (see also Pannella et al. 2009). Because the gas-phase metallicity also appears to be significantly correlated with stellar mass (and in the same direction as that observed for the mass–attenuation relation), it suggests a close connection between dust attenuation and gas-phase metallicity, in accord with expectations. Relating the mean obscuration in a given bin of stellar mass with the metallicity expected for that stellar mass from the mass-metallicity relation, we obtain the following empirical relation between obscuration and gas-phase metallicity as measured via the oxygen abundance:

$$12 + \log({\rm O/H}) = (0.18 \pm 0.03)\log(L_{\rm IR}/L_{\rm UV}) + (8.28 \pm 0.03) \quad \text{for } 1 \lesssim L_{\rm IR}/L_{\rm UV} \lesssim 40. \tag{6}$$

The upper limit to which the calibration is valid ($L_{\rm IR}/L_{\rm UV} \approx 40$) corresponds to the point at which [N II]/Hα begins to saturate for galaxies with close to solar metallicity (see next section). This conversion allows one to estimate to within 0.54 dex random scatter the gas-phase metallicity expected for a given dust attenuation for L^* galaxies at $z \sim 2$. This scatter includes both the scatter in the mass–metallicity relation (Erb et al. 2006a) and that in the relation between the [N II]/Hα ratio and oxygen abundance. This relation can be useful in practice because measuring the dust obscuration for large numbers of individual galaxies is observationally more feasible than measuring gas-phase metallicities; the latter requires near-IR spectroscopy at these redshifts. Nonetheless, we caution against the use of this relation for dust obscurations that are dissimilar to the ones used in the calibration, given the very limited dynamic range in metallicity probed by the current sample. Figure 18 shows the comparison between dust attenuation, stellar mass, and metallicity.

Recall that Equation (6) is derived from the average attenuation and metallicity of galaxies with a given stellar mass. To better gauge how well this relationship holds for individual galaxies, we examined sources in our sample that also have published individual metallicity determinations (see Table 9 of Law et al. 2009). To remove any potential systematics between metallicity calibrations, we considered only galaxies where oxygen

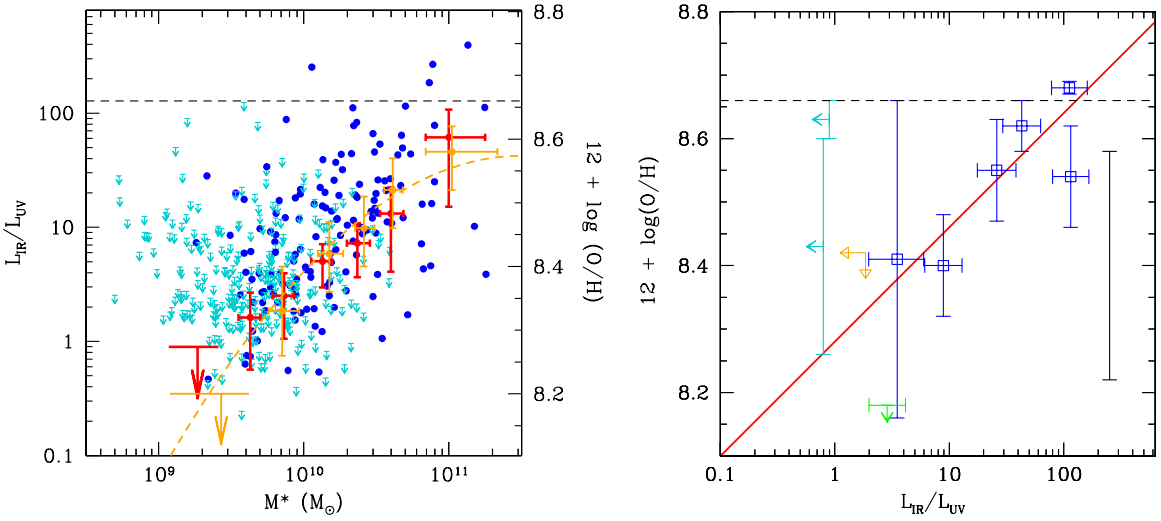

Figure 18. Left: dust attenuation, parameterized as L_{IR}/L_{UV}, as a function of stellar mass for 392 galaxies observed with MIPS. Galaxies detected and undetected at 24 μm are indicated by the circles and downward-pointing arrows, respectively. The average stacked values of the attenuation are indicated by the red points. The mass–metallicity relation from Erb et al. (2006a) is denoted by the orange points with the metallicity scale indicated on the right-hand axis. The mass–metallicity relation is scaled to match the stacked estimates for the attenuation according to Equation (6). The dashed horizontal line indicates solar metallicity (Asplund et al. 2004). Right: measurements of attenuation and oxygen abundance (derived from the N2 index; Pettini & Pagel 2004) for individual star-forming galaxies at $z \sim 2$. Points are color coded to reflect whether they have upper limits in attenuation and/or metallicity. The vertical black error bar denotes the random scatter between the [N II]/Hα ratio and oxygen abundance. The solid red line indicates the relation found by normalizing the mass–attenuation relation to match the mass–metallicity relation (left panel). The dashed horizontal line indicates solar metallicity (Asplund et al. 2004).

(A color version of this figure is available in the online journal.)

abundances were inferred from the N2 index (Pettini & Pagel 2004). While there were only 10 galaxies in our sample that met these requirements, their dust attenuations and metallicities are consistent with our conversion between the two within the measurement errors (≈0.12 dex scatter between the individual measurements and the relationship determined from stacking; Figure 18). Obviously, larger samples of galaxies with individual metallicity measurements, such as those made possible with multi-object near-IR spectrographs (e.g., MOSFIRE; McLean et al. 2008), will enable more detailed investigations of the connection between dust attenuation and gas-phase metallicity.

7.2. Comparison with the Local Relations

We can gain a broader perspective on the $z \sim 2$ results by comparing them to the local trend between metallicity and dust obscuration, where locally the galaxy metallicities are more robustly measured using a variety of calibrations and observations cover a larger dynamic range in metallicity. Heckman et al. (1998) find strong positive trends of oxygen abundance (O/H) with L_{IR}/L_{UV} and β for a sample of local starburst galaxies (Figure 19). They interpret these trends as a reflection of the increasing extinction of UV emission (and reddening of the UV slope) as the dust-to-gas ratio increases with gas-phase metallicity.

Before comparing with the $z \sim 2$ results, we must first account for the systematic differences in the way that oxygen abundances are inferred locally versus at high redshift (Kewley & Ellison 2008). As discussed above, the abundances for the $z \sim 2$ sample are derived based on the calibration of [N II]/Hα with O/H (Pettini & Pagel 2004). Alternatively, the abundances tabulated in Heckman et al. (1998) are based primarily on either direct temperature-sensitive (T_e) methods or the R23 calibration. For a robust comparison with the $z \sim 2$ sample, we searched the literature to find [N II]/Hα measurements for all of the Heckman et al. (1998) galaxies. The comparison between the metallicities tabulated in Heckman et al. (1998) and those derived from the N2 index is shown in Figure 19. The two sets of metallicity measurements agree well up to solar metallicity, at which point the [N II]/Hα indicator saturates due to nitrogen becoming the dominant coolant, an effect that has been noted elsewhere (Pettini & Pagel 2004; Kewley & Dopita 2002; Baldwin et al. 1981).

Having remeasured the metallicities for the local sample using the same abundance indicator adopted at high redshift, we find that the variations in O/H with β and IRX for L^* galaxies at $z \sim 2$ are in general agreement with the local relations (Figure 19). The implication of this agreement is that for a fixed metallicity, the $z \sim 2$ and $z \sim 0$ galaxies have similar dust-to-gas ratios, despite the fact that the high-redshift ones are 10–20 times more bolometrically luminous. It is here that we see another manifestation of the redshift evolution of the correlation between bolometric luminosity and dustiness. As discussed in Section 6, $z \sim 2$ galaxies are significantly more luminous at a fixed dust obscuration than local galaxies. We see a similar effect in the context of metallicity, in the sense that galaxies with a fixed metallicity (or dust-to-gas ratio) are significantly more luminous at high redshift. This result is a natural expectation given the positive correlation between dust attenuation and metallicity (Figure 19).

7.3. Bolometric Luminosity–Metallicity Relation at $z \sim 2$

The progression of metallicity with increasing obscuration (Figures 18) and the strong correlation between bolometric luminosity and dust attenuation (Section 6) imply the existence of a luminosity–metallicity relation at $z \sim 2$ (e.g., see also Erb et al. 2006a; Shapley et al. 2004). Further, the similarity in dust-to-gas ratio and difference in luminosity suggests a significant redshift evolution in the optical luminosity–metallicity relation, as has been noted by Erb et al. (2006a) and Shapley et al. (2004) in the context of $z \sim 2$ galaxies, and noted elsewhere for samples primarily at lower redshift (e.g., Kobulnicky & Kewley 2004; Kobulnicky et al. 2003; Maier et al. 2006, 2004;

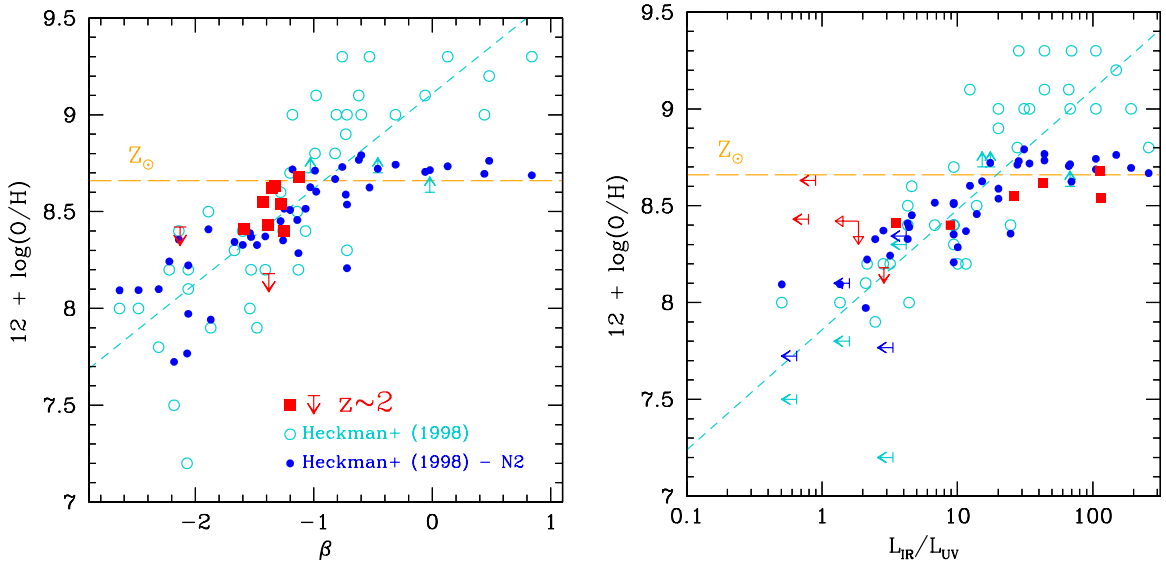

Figure 19. Left: oxygen abundance vs. UV slope, β, for galaxies at $z \sim 2$. For comparison, data for local starburst galaxies from Heckman et al. (1998) are provided, both using the original metallicity calibrations of that study (open circles) and updating their results for the [N II]/Hα-derived metallicity (filled circles). Their best-fit linear relation (for the original data) is indicated by the short-dashed line. The long-dashed line denotes solar metallicity (Asplund et al. 2004). Right: same as left panel for oxygen abundance vs. dust obscuration, $L_{\rm IR}/L_{\rm UV}$.

(A color version of this figure is available in the online journal.)

Salzer et al. 2005; Lara-Lopez et al. 2009). Quantitatively, an LIRG with $L_{\rm bol} \sim 10^{11}\ L_\odot$ at $z \sim 2$ is on average a third less metal enriched than a galaxy with the same (LIRG) bolometric luminosity locally. Similarly, the results suggest that high-redshift galaxies are scaled up versions of local starbursts where, for a fixed metallicity, the high-redshift ones are significantly more luminous than the local ones.

These observations can be understood if high-redshift galaxies are on average less evolved than local galaxies, where the high-redshift ones have larger gas fractions and are forming stars in a less metal-rich environment (e.g., Erb et al. 2006a; Reddy et al. 2006b). The redshift evolution of both the luminosity–metallicity and the luminosity–obscuration relations is then largely reflective of the underlying chemical evolution of galaxies as they age. As we have seen (Section 6), this evolution has important implications for the relative transparency (or "optical depth") of galaxies and their amenability to UV selection at ever-increasing redshifts.

8. CONCLUSIONS

We use ground-based UV imaging, near-IR spectroscopy, and *Spitzer* MIPS 24 μm imaging of a large sample of LBGs to investigate how the 8 μm luminosity (L_8) is related to the Hα luminosity (L(Hα)), infrared luminosity ($L_{\rm IR}$), and SFR of L^* galaxies at $z \sim 2$. *Chandra* X-ray data are used to provide an independent check of the average SFRs derived in this manner. We then use the derived relationships to estimate the bolometric luminosities ($L_{\rm bol}$) and dust attenuation of typical galaxies at $z \sim 2$. Our main conclusions are as follows.

1. Using a sample of 90 LBGs with Hα spectroscopic and narrowband observations and MIPS 24 μm imaging, we find a tight correlation between L_8 and L(Hα) with 0.24 dex scatter. We combine this result with the Kennicutt relations, taking care to account for the unobscured component of the star formation rate, to derive relations between L_8 and $L_{\rm IR}$/SFR.
2. Based on a larger sample of 392 galaxies with MIPS observations, we find that the rest-frame UV slopes (β) of typical star-forming galaxies at $z \sim 2$ with ages $\gtrsim$100 Myr correlate significantly with dust attenuation, parameterized by the ratio of infrared-to-UV luminosity, $L_{\rm IR}/L_{\rm UV}$. Galaxies with flatter (bluer) β are less dusty on average than those with redder β. Further, the correlation between β and dust attenuation is indistinguishable from that established for local UV-starburst galaxies (Meurer et al. 1999; Calzetti et al. 2000), the latter of which is almost always used to infer the dust attenuation of UV-selected galaxies at high redshift. We demonstrate here that the local correlation can be used to infer the extinction and bolometric luminosities of $10^{10}\ L_\odot \lesssim L_{\rm IR} \lesssim 10^{12}\ L_\odot$ galaxies at $z \sim 2$ to within a scatter of 0.4 dex. Galaxies with the largest bolometric luminosities of $L_{\rm bol} \gtrsim 10^{12}\ L_\odot$ have bluer β than their dust attenuations would imply based on the local correlation, or the correlation for the vast majority of star-forming galaxies at $z \sim 2$. This effect is likely due to the fact that the majority of the star formation in these bolometrically luminous and heavily attenuated galaxies is optically thick at UV wavelengths (see also point 5 below).
3. Separately, $\lesssim$13% of our $z \sim 2$ sample consists of young galaxies with inferred ages of $\lesssim$100 Myr. Unlike their older and more typical counterparts, these young galaxies are significantly less attenuated at a given β, as evidenced by their larger nondetection rate at 24 μm and their nondetections in the stacked 24 μm and X-ray images. These observations suggest that young galaxies may follow an extinction curve that is different than the usually assumed Meurer/Calzetti; the data for the young galaxies are consistent with an SMC-like extinction curve. If this is the case, then their dust obscuration may be up to a factor of 2–3 lower than the values obtained by assuming the local correlation between β and dust attenuation.
4. We verify our previous result that galaxies with larger bolometric luminosities are more heavily attenuated by dust, and

galaxies with redder β are also more bolometrically luminous on average than those with bluer β. Comparison with the local correlation between $L_{\rm bol}$ and dust attenuation implies that L^* galaxies at $z \sim 2$ with $L_{\rm bol} \sim 10^{11}\ L_\odot$ are an order of magnitude less dusty than local galaxies with a similar $L_{\rm bol}$. Such an effect may be related to an increase of dust-to-gas ratio as galaxies age. The redshift evolution in the extinction per unit SFR implies that in practice UV selection gives access to galaxies with an increasingly larger range in $L_{\rm bol}$ at increasing redshift. It also implies that the UV SED alone can be used to recover the total dust attenuation in galaxies with progressively larger $L_{\rm bol}$ at higher redshift, given that, at higher redshift, galaxies are more transparent in the UV at a fixed $L_{\rm bol}$.

5. We recast the correlation between bolometric luminosity and dust attenuation at $z \sim 2$ in terms of observed UV luminosity to come to the following conclusions. First, galaxies with faint UV luminosities are expected to be less attenuated than their UV-bright counterparts. This result is supported by our data that indicate that UV-faint galaxies are less IR luminous (and less bolometrically luminous) than UV-bright ones. Second, we observe that galaxies with very large SFRs (e.g., ULIRGs) are less UV luminous per unit SFR than galaxies with lower SFRs (e.g., LIRGs), implying that the dust covering fraction is likely increasing more rapidly with SFR than the intrinsic UV luminosity. This effect results in a saturation of the UV luminosity. This saturation occurs at the value of L^* at these redshifts, implying that the bright end of the UV LF at $z \sim 2$ is likely modulated by dust obscuration.
6. Motivated by the expectation of a direct correspondence between extinction and metallicity, we have examined the relationship between dust attenuation and stellar mass. Galaxies with stellar mass $\gtrsim 10^{11}\ M_\odot$ are almost 100 times more dusty on average than those with masses $\lesssim 10^{9.5}\ M_\odot$. The monotonically increasing mass–attenuation and mass–metallicity relations imply a close connection between attenuation and metallicity, allowing us to provide an empirical calibration between the two. This calibration is verified with a small sample of $z \sim 2$ galaxies with individual metallicity determinations. Comparison with the local relationship between metal abundance and dust obscuration suggests that L^* galaxies at $z \sim 2$ have a similar ratio of dust to metals as local starbursts, despite the high-redshift galaxies' bolometric luminosities being a factor of 10–20 times larger than local galaxies. Our results imply a redshift evolution in the luminosity–metallicity and luminosity–obscuration relations that reflects the underlying chemical evolution of galaxies as they age.

We have utilized all the data at our disposal, including UV imaging, Hα narrowband and spectroscopic observations, and *Spitzer* MIPS 24 μm imaging, to investigate the viability of rest-frame 8 μm luminosity as a SFR and dust indicator. We go on to show how these data indicate that the UV slopes of high-redshift galaxies are sensitive to dust in the same way as they are in the local universe; thus the UV slope is an important proxy for inferring the bolometric luminosities of high-redshift galaxies in the absence of longer wavelength data. Further analysis will benefit from observations with near-IR multi-object spectrographs allowing simultaneous coverage of at least two near-IR bands, which will enable direct measurements of the nebular reddening via the Balmer decrement for $z \sim 2$ galaxies. Future observations with the *Herschel* Space Telescope will no doubt greatly extend our results. These new observations will directly sample the longer wavelength (rest frame 30 μm) dust emission of at least luminous LIRGs at $z \sim 2$, and will yield more robust measurements of the bolometric luminosities of more typical galaxies at $z \sim 2$.

We thank the staff of the Keck and Palomar Observatories for their help in obtaining the data presented here. Support for N.A.R. was provided by NASA through Hubble Fellowship grant HST-HF-01223.01 awarded by the Space Telescope Science Institute, which is operated by the Association of Universities for Research in Astronomy, Inc., for NASA, under contract NAS 5-26555. Additional support has been provided by research funding for the *Spitzer Space Telescope* Legacy Science Program, provided by NASA through contracts 1224666 and 1287778, issued by the Jet Propulsion Laboratory, California Institute of Technology. C.C.S. has been supported by grants AST 03-07263 and AST 06-06912 from the National Science Foundation and by the David and Lucile Packard Foundation.

REFERENCES

Adelberger, K. L., & Steidel, C. C. 2000, ApJ, 544, 218
Adelberger, K. L., Steidel, C. C., Shapley, A. E., Hunt, M. P., Erb, D. K., Reddy, N. A., & Pettini, M. 2004, ApJ, 607, 226
Alexander, D. M., et al. 2003, AJ, 126, 539
Asplund, M., Grevesse, N., Sauval, A. J., Allende Prieto, C., & Kiselman, D. 2004, A&A, 417, 751
Baker, A. J., Lutz, D., Genzel, R., Tacconi, L. J., & Lehnert, M. D. 2001, A&A, 372, L37
Baldwin, J. A., Phillips, M. M., & Terlevich, R. 1981, PASP, 93, 5
Bavouzet, N., Dole, H., Le Floc'h, E., Caputi, K. I., Lagache, G., & Kochanek, C. S. 2008, A&A, 479, 83
Bell, E. F. 2003, ApJ, 586, 794
Bouwens, R. J., et al. 2009, ApJ, 705, 936
Brandl, B. R., et al. 2006, ApJ, 653, 1129
Brinchmann, J., Charlot, S., White, S. D. M., Tremonti, C., Kauffmann, G., Heckman, T., & Brinkmann, J. 2004, MNRAS, 351, 1151
Bruzual, G., & Charlot, S. 2003, MNRAS, 344, 1000
Buat, V., Marcillac, D., Burgarella, D., Le Floc'h, E., Takeuchi, T. T., Iglesias-Paràmo, J., & Xu, C. K. 2007, A&A, 469, 19
Buat, V., Takeuchi, T. T., Burgarella, D., Giovannoli, E., & Murata, K. L. 2009, A&A, 507, 693
Buat, V., et al. 2007, ApJS, 173, 404
Burgarella, D., Buat, V., Takeuchi, T. T., Wada, T., & Pearson, C. 2008, in ASP Conf. Ser. 381, The Second Annual Spitzer Science Center Conference Infrared Diagnostics of Galaxy Evolution, ed. R.-R. Chary, H. I. Teplitz, & K. Sheth (San Francisco, CA: ASP), 203
Calzetti, D., Armus, L., Bohlin, R. C., Kinney, A. L., Koornneef, J., & Storchi-Bergmann, T. 2000, ApJ, 533, 682
Caputi, K. I., et al. 2007, ApJ, 660, 97
Chabrier, G. 2003, PASP, 115, 763
Chapman, S. C., Blain, A. W., Smail, I., & Ivison, R. J. 2005, ApJ, 622, 772
Chapman, S. C., & Casey, C. M. 2009, MNRAS, 1216
Chary, R., & Elbaz, D. 2001, ApJ, 556, 562
Conroy, C., Shapley, A. E., Tinker, J. L., Santos, M. R., & Lemson, G. 2008, ApJ, 679, 1192
Daddi, E., et al. 2007, ApJ, 670, 156
Elbaz, D., Cesarsky, C. J., Chanial, P., Aussel, H., Franceschini, A., Fadda, D., & Chary, R. R. 2002, A&A, 384, 848
Engelbracht, C. W., Gordon, K. D., Rieke, G. H., Werner, M. W., Dale, D. A., & Latter, W. B. 2005, ApJ, 628, L29
Epinat, B., et al. 2009, A&A, 504, 789
Erb, D. K., Shapley, A. E., Pettini, M., Steidel, C. C., Reddy, N. A., & Adelberger, K. L. 2006a, ApJ, 644, 813
Erb, D. K., Steidel, C. C., Shapley, A. E., Pettini, M., Reddy, N. A., & Adelberger, K. L. 2006b, ApJ, 647, 128
Erb, D. K., Steidel, C. C., Shapley, A. E., Pettini, M., Reddy, N. A., & Adelberger, K. L. 2006c, ApJ, 646, 107
Förster Schreiber, N. M., Roussel, H., Sauvage, M., & Charmandaris, V. 2004, A&A, 419, 501
Förster Schreiber, N. M., et al. 2009, ApJ, 706, 1364

Frayer, D. T., et al. 2006, AJ, 131, 250
Galliano, F., Dwek, E., & Chanial, P. 2008, ApJ, 672, 214
Ghosh, P., & White, N. E. 2001, ApJ, 559, L97
Giavalisco, M., Koratkar, A., & Calzetti, D. 1996, ApJ, 466, 831
Goldader, J. D., Meurer, G., Heckman, T. M., Seibert, M., Sanders, D. B., Calzetti, D., & Steidel, C. C. 2002, ApJ, 568, 651
Grimes, J. P., Heckman, T., Hoopes, C., Strickland, D., Aloisi, A., Meurer, G., & Ptak, A. 2006, ApJ, 648, 310
Grimes, J. P., Heckman, T., Strickland, D., & Ptak, A. 2005, ApJ, 628, 187
Heckman, T. M., Robert, C., Leitherer, C., Garnett, D. R., & van der Rydt, F. 1998, ApJ, 503, 646
Helou, G., Malhotra, S., Hollenbach, D. J., Dale, D. A., & Contursi, A. 2001, ApJ, 548, L73
Hogg, D. W., Tremonti, C. A., Blanton, M. R., Finkbeiner, D. P., Padmanabhan, N., Quintero, A. D., Schlegel, D. J., & Wherry, N. 2005, ApJ, 624, 162
Huang, J.-S., et al. 2009, ApJ, 700, 183
Isobe, T., Feigelson, E. D., & Nelson, P. I. 1986, ApJ, 306, 490
Kennicutt, R. C. 1998, ARA&A, 36, 189
Kennicutt, R. C., et al. 2009, ApJ, 703, 1672
Kewley, L. J., & Dopita, M. A. 2002, ApJS, 142, 35
Kewley, L. J., & Ellison, S. L. 2008, ApJ, 681, 1183
Kinney, A. L., Bohlin, R. C., Calzetti, D., Panagia, N., & Wyse, R. F. G. 1993, ApJS, 86, 5
Kobulnicky, H. A., & Kewley, L. J. 2004, ApJ, 617, 240
Kobulnicky, H. A., et al. 2003, ApJ, 599, 1006
Kotak, R., et al. 2009, ApJ, 704, 306
Lara-Lopez, M. A., Cepa, J., Bongiovanni, A., Perez Garcia, A. M., Castaneda, H., Fernandez Lorenzo, M., Povic, M., & Sanchez-Portal, M. 2009, A&A, 505, 529
Law, D. R., Steidel, C. C., Erb, D. K., Larkin, J. E., Pettini, M., Shapley, A. E., & Wright, S. A. 2009, ApJ, 697, 2057
Law, D. R., Steidel, C. C., Erb, D. K., Pettini, M., Reddy, N. A., Shapley, A. E., Adelberger, K. L., & Simenc, D. J. 2007, ApJ, 656, 1
Leitherer, C. 2008, in IAU Symp. 255, Low-Metallicity Star Formation: From the First Stars to Dwarf Galaxies, ed. L. K. Hunt, S. Madden, & R. Schneider (Dordrecht: Kluwer), 305
Madau, P. 1995, ApJ, 441, 18
Madau, P., Ferguson, H. C., Dickinson, M. E., Giavalisco, M., Steidel, C. C., & Fruchter, A. 1996, MNRAS, 283, 1388
Maier, C., Lilly, S. J., Carollo, C. M., Meisenheimer, K., Hippelein, H., & Stockton, A. 2006, ApJ, 639, 858
Maier, C., Meisenheimer, K., & Hippelein, H. 2004, A&A, 418, 475
Maiolino, R., Schneider, R., Oliva, E., Bianchi, S., Ferrara, A., Mannucci, F., Pedani, M., & Roca Sogorb, M. 2004, Nature, 431, 533
Makovoz, D., & Marleau, F. R. 2005, PASP, 117, 1113
Marigo, P., & Girardi, L. 2007, A&A, 469, 239
McLean, I. S., Steidel, C. C., Matthews, K., Epps, H., & Adkins, S. M. 2008, Proc. SPIE, 7014, 99
Meurer, G. R., Heckman, T. M., & Calzetti, D. 1999, ApJ, 521, 64
Nandra, K., Mushotzky, R. F., Arnaud, K., Steidel, C. C., Adelberger, K. L., Gardner, J. P., Teplitz, H. I., & Windhorst, R. A. 2002, ApJ, 576, 625
Normand, P., Rouan, D., Lacombe, F., & Tiphene, D. 1995, A&A, 297, 311
Pannella, M., et al. 2009, ApJ, 698, L116
Papovich, C., Dickinson, M., & Ferguson, H. C. 2001, ApJ, 559, 620
Papovich, C., et al. 2006, ApJ, 640, 92
Papovich, C., et al. 2007, ApJ, 668, 45
Pettini, M., Kellogg, M., Steidel, C. C., Dickinson, M., Adelberger, K. L., & Giavalisco, M. 1998, ApJ, 508, 539
Pettini, M., & Pagel, B. E. J. 2004, MNRAS, 348, L59
Pilyugin, L. S., Vílchez, J. M., & Contini, T. 2004, A&A, 425, 849
Puget, J. L., & Leger, A. 1989, ARA&A, 27, 161
Ranalli, P., Comastri, A., & Setti, G. 2003, A&A, 399, 39
Reddy, N. A., Erb, D. K., Steidel, C. C., Shapley, A. E., Adelberger, K. L., & Pettini, M. 2005, ApJ, 633, 748
Reddy, N. A., & Steidel, C. C. 2004, ApJ, 603, L13
Reddy, N. A., & Steidel, C. C. 2009, ApJ, 692, 778
Reddy, N. A., Steidel, C. C., Erb, D. K., Shapley, A. E., & Pettini, M. 2006a, ApJ, 653, 1004
Reddy, N. A., Steidel, C. C., Fadda, D., Yan, L., Pettini, M., Shapley, A. E., Erb, D. K., & Adelberger, K. L. 2006b, ApJ, 644, 792
Reddy, N. A., Steidel, C. C., Pettini, M., Adelberger, K. L., Shapley, A. E., Erb, D. K., & Dickinson, M. 2008, ApJS, 175, 48
Rigby, J. R., et al. 2008, ApJ, 675, 262
Roussel, H., Sauvage, M., Vigroux, L., & Bosma, A. 2001, A&A, 372, 427
Salzer, J. J., Lee, J. C., Melbourne, J., Hinz, J. L., Alonso-Herrero, A., & Jangren, A. 2005, ApJ, 624, 661
Sawicki, M., & Yee, H. K. C. 1998, AJ, 115, 1329
Seibert, M., Heckman, T. M., & Meurer, G. R. 2002, AJ, 124, 46
Shapley, A. E., Erb, D. K., Pettini, M., Steidel, C. C., & Adelberger, K. L. 2004, ApJ, 612, 108
Shapley, A. E., Steidel, C. C., Adelberger, K. L., Dickinson, M., Giavalisco, M., & Pettini, M. 2001, ApJ, 562, 95
Shapley, A. E., Steidel, C. C., Erb, D. K., Reddy, N. A., Adelberger, K. L., Pettini, M., Barmby, P., & Huang, J. 2005, ApJ, 626, 698
Siana, B., Teplitz, H. I., Chary, R.-R., Colbert, J., & Frayer, D. T. 2008, ApJ, 689, 59
Siana, B., et al. 2009, ApJ, 698, 1273
Stark, A. A., Gammie, C. F., Wilson, R. W., Bally, J., Linke, R. A., Heiles, C., & Hurwitz, M. 1992, ApJS, 79, 77
Steidel, C. C., Adelberger, K. L., Giavalisco, M., Dickinson, M., & Pettini, M. 1999, ApJ, 519, 1
Steidel, C. C., Adelberger, K. L., Shapley, A. E., Erb, D. K., Reddy, N. A., & Pettini, M. 2005, ApJ, 626, 44
Steidel, C. C., Adelberger, K. L., Shapley, A. E., Pettini, M., Dickinson, M., & Giavalisco, M. 2003, ApJ, 592, 728
Steidel, C. C., Pettini, M., & Hamilton, D. 1995, AJ, 110, 2519
Steidel, C. C., Shapley, A. E., Pettini, M., Adelberger, K. L., Erb, D. K., Reddy, N. A., & Hunt, M. P. 2004, ApJ, 604, 534
Steidel, C. C., et al. 2010, ApJ, submitted
Strickland, D. K., Heckman, T. M., Colbert, E. J. M., Hoopes, C. G., & Weaver, K. A. 2004, ApJ, 606, 829
Tielens, A. G. G. M., Hony, S., van Kerckhoven, C., & Peeters, E. 1999, in The Universe as Seen by ISO, ed. P. Cox & M. F. Kessler (ESA-SP 427; Noordwijk: ESA), 579
Todini, P., & Ferrara, A. 2001, MNRAS, 325, 726
Tremonti, C. A., et al. 2004, ApJ, 613, 898
Vila Costas, M. B., & Edmunds, M. G. 1992, MNRAS, 259, 121
Wang, B., & Heckman, T. M. 1996, ApJ, 457, 645
Wu, H., Cao, C., Hao, C.-N., Liu, F.-S., Wang, J.-L., Xia, X.-Y., Deng, Z.-G., & Young, C. K.-S. 2005, ApJ, 632, L79
Zaritsky, D., Kennicutt, Jr., R. C., & Huchra, J. P. 1994, ApJ, 420, 87
Zoran, O., Barkana, R., & Thompson, R. I. 2006, MNRAS, 368, L47